Interacting effects of droplet number and ice formation processes on mixed-phase cold-air outbreak clouds

Xinyi Huang[1], Paul R. Field[1,2], Ross J. Herbert[1], Benjamin J. Murray[1], Floortje van den Heuvel[3], Daniel P. Grosvenor[1,2], Rachel W. N. Sansom[1], and Kenneth S. Carslaw[1]

[1]Institute for Climate and Atmospheric Science, School of Earth and Environment, University of Leeds, Leeds LS2 9JT, United Kingdom
[2]Met Office, Exeter EX1 3PB, United Kingdom
[3]British Antarctic Survey, Cambridge CE3 0ET, United Kingdom

Correspondence: Xinyi Huang (ee21xh@leeds.ac.uk)

Abstract. Shallow, mixed-phase clouds associated with cold-air outbreak (CAO) events are natural laboratories for studying mixed-phase cloud processes which are important for estimating cloud-phase feedback in the warming climate. Recent studies show that CAO clouds are sensitive to aerosol-cloud interactions and ice formation processes, but many modelling studies perturbed model parameters individually, limiting the investigation of joint effects from multiple processes on cloud properties.

5 Here we investigated how six cloud microphysics parameters jointly affect CAO cloud properties by building model emulators trained on output from perturbed parameter ensembles of a high-resolution regional model. The parameters are cloud droplet number concentration (N_d), ice-nucleating particle concentration (N_{INP}), efficiencies of three secondary ice production processes, as well as the mixed-phase overlap factor (mpof). For the CAO case studied, N_d and N_{INP} most strongly control the cloud radiative properties in the stratocumulus region; whereas in the cumulus region, effects from varying N_d and mpof are

10 the strongest. Our results show that these parameters have non-linear joint effects such that the magnitude and even sign of cloud responses to a parameter are highly dependent on the values of other parameters. For example, the sensitivity of cloud albedo to increases in N_{INP} varies between near zero to strongly negative across the sampled parameter space. Therefore, perturbing parameters individually is an inadequate method for determining the cloud responses to model parameters. This work demonstrates the power of model emulation and the importance of a full exploration of parameter space in order to understand

15 the factors controlling cloud properties.

1 Introduction

Low-level, mixed-phase clouds at mid and high latitudes play a key role in the low-cloud optical depth feedback through their phase changes in a warming climate and affect the Earth's radiation budget (Ceppi et al., 2017), which is referred to as the cloud-phase feedback (Mitchell et al., 1989; Storelvmo et al., 2015; Ceppi et al., 2017; Murray et al., 2021). In these mixed-phase

20 clouds, liquid and ice hydrometeors exist at the same time, and the radiative properties of these clouds are strongly controlled by the characteristics and interactions of these hydrometeors at the microphysical scale (Korolev et al., 2017). However, because current global climate models are generally poor in representing mixed-phase cloud microphysics (Bodas-Salcedo et al., 2019;

Sherwood et al., 2020), uncertainties persist in both the direction and magnitude of the cloud-phase feedback (Sherwood et al., 2020; Zelinka et al., 2020; Forster et al., 2021; Murray et al., 2021). In fact, cloud microphysical processes are subject to large
25 uncertainties due to their highly parametrized and complicated nature (Morrison et al., 2020), even within high-resolution models such as cloud-resolving models and large-eddy simulations.

In this study, we focused on a specific synoptic-scale meteorological event called a cold-air outbreak (CAO). During a CAO event, air masses flow from cold and dry high-latitude continents or ice-covered regions to the warm, open and sea-ice free ocean, leading to instability of the marine boundary layer and strong atmospheric convection for cloud formation
30 (Brümmer, 1996; Brümmer, 1999; Renfrew and Moore, 1999; Kolstad and Bracegirdle, 2008; Kolstad et al., 2009; Fletcher et al., 2016a, b). As the temperature during CAO events is low and normally below 0 °C, extensive mixed-phase clouds form. These mixed-phase CAO clouds have a well-defined flow, which makes them ideal natural laboratories for understanding the mixed-phase processes that are important for modelling the behaviour of mixed-phase clouds under the warming climate. The CAO clouds usually begin with a form of "cloud street" or stratocumulus-like clouds, and then transition into cumulus-like
35 clouds downwind (Brümmer, 1999; McCoy et al., 2017), which can have very different radiative properties (McCoy et al., 2017).

Cloud microphysics strongly controls mixed phase CAO cloud properties. Several high-resolution modelling studies have been conducted to understand the effect of various cloud microphysics processes and parameters on CAO clouds (Field et al., 2014; Abel et al., 2017; Vergara-Temprado et al., 2018; de Roode et al., 2019; Tornow et al., 2021; Karalis et al., 2022;
40 Li et al., 2023; Possner et al., 2024; Huang et al., 2025). These studies show that the cloud properties are very sensitive to aerosols including those that can act as cloud condensation nuclei (CCN) and ice-nucleating particles (INPs), as well as ice formation processes including primary ice production and secondary ice production (SIP). However, all of these studies were conducted by perturbing parameters individually, often called a one-at-a-time (OAT) sensitivity approach. Such an OAT test only allows the responses of cloud properties around a control simulation to be quantified, lacking full exploration of the
45 parameter space and interactions between the parameters. For example, Johnson et al. (2015) has shown that the responses of modelled precipitation in deep convective clouds to the concentration of Aitken and accumulation modes of aerosols and the collection efficiency of drops by graupel are strongly dependent on the values of each other.

A large number of simulations are needed to explore multiple combinations of parameters, which is computationally expensive and impractical for a large number of parameters. To obtain the responses of model variables over the whole parameter
50 space, we applied the approach of model emulation with Gaussian Process (GP) emulators, which is a Bayesian machine learning approach that statistically learns the relationship between model inputs and outputs and acts as a surrogate model of the complex numerical model (Oakley and O'Hagan, 2002; O'Hagan, 2006). The training data are produced by running PPE (perturbed parameter ensemble) simulations of a numerical model, where parameters are perturbed in combinations that are well-designed for training the emulators. The model emulation approach has been recently applied in many complex climate
55 and atmospheric models, including understanding the magnitude and causes of uncertainty in aerosol radiative forcing (Lee et al., 2011, 2012, 2013; Regayre et al., 2014, 2015, 2018; Lee et al., 2016; Johnson et al., 2018; Marshall et al., 2019), assessing potential model simplification of cloud microphysics in global climate models (Proske et al., 2022, 2023), constraining

model parametric uncertainties with observations (Johnson et al., 2020; Regayre et al., 2023) and identifying the potential existence of structural deficiencies in climate models (Regayre et al., 2023; Prévost et al., 2025). Besides global models, this approach has also been used in regional models such as investigating the environmental controls on sea breeze circulations (Igel et al., 2018; Park et al., 2020), understanding the controls of cloud properties for deep convective clouds (Johnson et al., 2015; Wellmann et al., 2018, 2020; Hawker et al., 2021) and stratocumulus clouds (Glassmeier et al., 2019; Sansom, 2021; Sansom et al., 2024, 2025). With the model response surface generated from the GP emulators, a variance-based sensitivity analysis (Saltelli et al., 2000) can be applied to quantify the sensitivities of model variables to the investigated parameters.

Here we focus on the influences of aerosol-cloud interactions and ice formation processes on a CAO cloud system over the Labrador Sea on 24 October 2022. This is the warmer case studied in our previous OAT test work (Huang et al., 2025), which showed similar cloud responses to previous studies of aerosol-cloud interactions and ice formation processes in CAO clouds. We explore the joint effects of 6 parameters: (1) fixed in-cloud droplet number concentration, (2) INP concentration, (3-5) three parameters from SIP processes including the Hallett-Mossop process, ice-ice collision and droplet shattering, as well as (6) a parameter controlling the extent of spatial overlap between liquid and ice clouds. The parameters for ice-ice collision, droplet shattering and the extent of spatial overlap between liquid and ice clouds are additional to the parameters studied in Huang et al. (2025). All three SIP mechanisms have been shown to be important for CAO cloud morphology (Karalis et al., 2022) and ice crystal number concentrations in Arctic stratocumulus clouds (Sotiropoulou et al., 2020). It is also suggested that changing the degree of spatial overlap between liquid and ice, which can be estimated with observations, can exert a strong influence on the liquid water path (LWP) and radiative properties of mixed-phase CAO clouds (Abel et al., 2017; Evans et al., 2025).

This paper is structured as follows. In Section 2, we describe the numerical model setup, PPE design, training, validation and testing of the GP emulators. In Section 3, we present the results starting with example PPE output, and then emulated model responses from the emulators, as well as the multiple OAT tests across the whole parameter space from emulators, followed by summary and discussion on the results of our study compared to previous work, limitations of this study and potential future work in Section 4.

2 Methods

Our overall approach was to use PPEs (perturbed parameter ensembles) and GP (Gaussian Process) emulators to understand the joint effects of six cloud microphysics parameters at different stages of a CAO (cold-air outbreak) event. A flow chart of methods involved in this work is shown in Appendix D.

2.1 Model setup and case description

The nested UM (Unified Model) (Brown et al., 2012a) from the UK Met Office was coupled with a double-moment cloud microphysics scheme CASIM (Cloud AeroSol Interacting Microphysics) (Field et al., 2023). We used UM version 13.0 with the RAL (Regional Atmosphere and Land) 3.2 configuration (Bush et al., 2025). The boundary conditions of the nested domains were provided hourly by a global model (N216) with the GAL (Global Atmosphere and Land) 6.1 configuration (Walters et al., 2017). The cloud parameterization in the nested model was from the Bimodal Cloud scheme (Weverberg et al., 2021b, a), and the radiative processes were from SOCRATES (Suite Of Community Radiative Transfer codes based on Edwards and Slingo) (Manners et al., 2023). Mass mixing ratio and number concentration of ice hydrometeors were both considered when calculating the single-scattering albedo of ice in SOCRATES (Baran et al., 2025). The parameterization of boundary layer processes in our model is from Lock et al. (2000).

The selected CAO event occurred on 24 October 2022 over the Labrador Sea, which coincided with two flights (C322 and C323) during the M-Phase aircraft campaign (Murray and the M-Phase Team, 2024; Clarke et al., 2025). Figure 1 shows the tracks of both flights, the corresponding nested model domains, and the analysis domains. Flight C322 measured regions dominated by stratocumulus (Sc) clouds, while Flight C323 focused on regions dominated by cumulus (Cu) clouds.

Both nested model domains contain 500×500 gridpoints with a horizontal grid spacing of 1.5 km, centred at 60 °N, 60.5 °W for capturing the early stage and Sc region and 56 °N, 51 °W for the Cu region. Field et al. (2017) has demonstrated that this grid spacing is capable of reproducing the general cloud features of a CAO event. The nested model domains were designed to ensure the model analysis domains remained sufficiently distant from the domain boundaries, allowing cloud fields to fully develop when they leave the ice edge and before entering the model analysis domains. At this point, the model has already spun up from the boundaries. The regional model has 90 vertical levels capped at 40 km with 16 model levels below 1 km and 28 model levels below 3 km.

The simulations were initialized at 0000 UTC and performed for 24 hours, with the model output from the first 12 hours excluded from the analysis due to model spin-up.

2.2 Perturbed parameters and PPE design

Six parameters were investigated in this study: N_d (cloud droplet number concentration), N_{INP}^{-15} (INP concentration at -15 °C), E_{HM} (efficiency of the Hallett-Mossop process), E_{BR} (leading coefficient controlling the efficiency of the ice-ice collisional breakup process), E_{DS} (efficiency of the droplet shattering process), and mpof (mixed-phase overlap factor). All the parameters are within the CASIM scheme. A description of each perturbed parameter and the selection of their perturbed ranges are
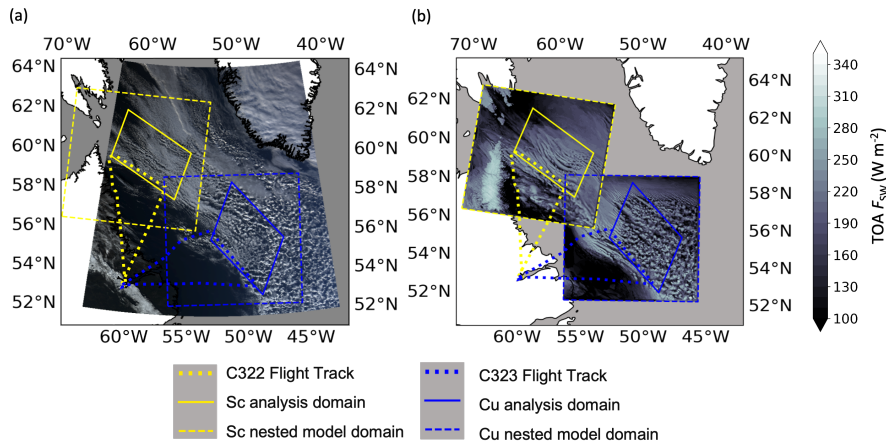
Figure 1. Flight tracks (dotted line), nested model domains (dashed squares) and model analysis domains (solid rectangles) for Sc region (yellow) and Cu region (blue) on 24 October 2022 over the Labrador Sea: (a) the RGB satellite imagery created using bands 1 (620-670 nm), 3 (459-479 nm) and 4 (545-565 nm) from MODIS (Moderate Resolution Imaging Spectroradiometer) Level 1B Calibrated Radiances Product (Collection 6.1) (MODIS Characterization Support Team (MCST), 2017) onboard the Aqua satellite, (b) the SW (shortwave) reflectance at the top-of-the-atmosphere from the control simulations. The selected model time is the same as the satellite retrieval time at 17:00 UTC and the model output fields are instantaneous.

introduced in this section. The combinations of the six parameter values were designed with the maximin Latin hypercube sampling method. The single OAT test was performed for every parameter before running the PPEs to investigate the effects of perturbing each parameter individually around the control simulation (not shown).

Figure 2 shows the main processes in CASIM with relevant processes for the perturbed parameters in this work highlighted. Not all processes in CASIM are shown here (e.g., self-collection, sedimentation, evaporation and sublimation); see Field et al. (2023) for a complete description of CASIM implementation in the UM. To keep the consistency of symbols, we used the same symbol for mass tendency (P) and number tendency (N) in the description of parameters below.

2.2.1 N_d (cloud droplet number concentration)

N_d is a fixed vertical profile of in-cloud droplet number concentration set in CASIM if aerosols are not used for deriving the cloud droplet number concentration. We did not select the option to use aerosol-derived N_d in this study to avoid extra complexity for parameter perturbation and model output interpretation. N_d was set to 35 cm^{-3} in the control simulation and perturbed over the range from 5 cm^{-3} to 75 cm^{-3} in the PPE design to cover most of the observed N_d values from the CDP (cloud droplet probe) instrument onboard M-Phase C322 and C323 (Figure 3a). The 1 Hz CDP measurements were averaged to match the model resolution (1.5 km) and those with N_d less than 1 cm^{-3} were removed before averaging.

The range of N_d was chosen to understand how much the variation of N_d in a CAO event affects the cloud properties, which is uncertain in the modelling of in-cloud aerosol processing and limited by the fixed N_d setup. We did not select the bigger

5
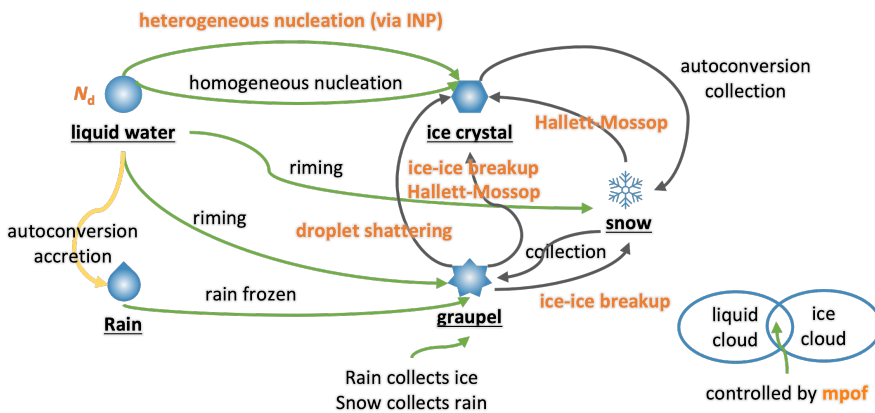
Figure 2. Key processes among the five CASIM hydrometeors: liquid water, rain, ice crystal, snow and graupel. Processes which contain the parameters investigated in this work are highlighted in orange. Liquid-liquid processes are highlighted in yellow, mixed-phase processes are highlighted in green and ice-ice processes are in dark grey. Details of the treatment of SIP processes are shown in the Methods section. Not all the cloud microphysical processes in CASIM are shown here; see Field et al. (2023) for detailed information about the implementation of CASIM in the UM.

range as in Huang et al. (2025) because the N_d at coarser resolution can be obtained from satellite retrievals (e.g., Grosvenor et al. (2018)), which is not the major source of uncertainties considered for this case in N_d.

2.2.2 N_{INP}^{-15} (INP concentration at -15 °C)

The INP concentrations over the Labrador Sea region were derived based on a new $n_s(T)$ (active site density) parameterization for soil dusts (Appendix A), to account for the biogenic component associated with the dust (Herbert et al., 2025). The dust concentrations from a global model over the Labrador Sea region during the M-Phase aircraft campaign period were used with the above soil dust parameterization to derive the temperature-dependent INP concentration perturbed in this study. Appendix B shows the details of the global model and the INP concentration in the control simulation which agrees well with INP measurements from the M-Phase aircraft campaign as in Figure 3c.

INP concentrations were perturbed by the same scale factor at all temperatures. For ease of reference to typical values we define the parameter in the PPE as N_{INP}^{-15} (INP concentration at -15 °C, L^{-1}), which is around 0.17 L^{-1} (170 m^{-3}) in the control simulation. The range of N_{INP}^{-15} in the PPE is shown in Figure 3b. The N_{INP}^{-15} were perturbed with a range from 1.7×10^{-5} L^{-1} (0.017 m^{-3}) to 17 L^{-1} (17000 m^{-3}) (factor of 0.0001 – 100 relative to the control value). Such big range of INP concentration (6 orders of magnitude) was selected to represent the uncertainties of INPs to our knowledge without the *in-situ* measurements of INPs from the aircraft campaign. This is because, unlike N_d, INP concentration cannot be derived from satellite/remote sensing.

2.2.3 E_{HM} (efficiency of the Hallett-Mossop process)

The Hallett-Mossop process (also called rime splintering) produces small ice splinters during the riming of liquid droplets onto existing ice hydrometeors (Hallett and Mossop, 1974). The efficiency of the Hallett-Mossop process (E_{HM}) is defined as the number of splinters produced per milligram of rimed liquid, with the mass of each splinter (M_{I0}) set as 10^{-18} kg. The mass tendency of ice created by the Hallett-Mossop process in CASIM (P_{ihal}) is based on the mass tendencies of graupel-cloud water (P_{gacw}) and snow-cloud water riming (P_{sacw}) with the number of splinters per milligram of rime varying according to a triangular function ($f(T)$) between -2.5 °C and -7.5 °C (outside of which the value is zero) with the peak at -5 °C (Field et al., 2023).

$$P_{ihal} = E_{HM} M_{I0} (P_{gacw} + P_{sacw}) f(T) \tag{1}$$

E_{HM} was set to 350 mg^{-1} in the control simulation and perturbed from 35 mg^{-1} to 3500 mg^{-1} (factor of $0.1 - 10$). This range was defined based on previous findings that simulations with a factor of 10 higher efficiency than the default value agree well with observed ice crystal number concentrations (Young et al., 2019). The lower limit was chosen to ensure that the default value remains sufficiently distant from the boundary of the parameter space, where emulator predictions are typically subject to higher uncertainties. The multiple OAT test (Section 3.3) and global sensitivity analysis (Appendix G) were performed with a different range of E_{HM} from the range of PPE design, which is from 350 mg^{-1} to 3500 mg^{-1} rather than from 10 mg^{-1} to 3500 mg^{-1}.

2.2.4 E_{BR} (coefficient controlling the efficiency of the ice-ice collisional breakup)

E_{BR} is a coefficient controlling the efficiency of the ice-ice collisional breakup (χ_{BR}), which is the number of fragments produced from hydrometeor collisions. The ice-ice collisional breakup parameterization used in this study follows the temperature-dependent approach in Takahashi et al. (1995) and Sullivan et al. (2018).

$$N_{iics,xy} = -\chi_{BR} N_{xacy} \tag{2}$$

$$\chi_{BR} = E_{BR} (T - T_{min})^{1.2} exp[-\frac{(T - T_{min})}{\gamma_{BR}}] \tag{3}$$

The minimum temperature (T_{min}) for ice-ice break-up is set at -21 °C and a decay rate (γ_{BR}) of fragment number at warmer subzero temperatures is set to 5. The collisions involve ice and snow particles breaking up through collisions with graupel. N_{xacy} are the existing number tendencies from graupel collecting ice and graupel collecting snow. Detailed description of mixed-phase and cold-phase collection between particles of different hydrometeors in CASIM can be found in Field et al. (2023).

E_{BR} was set to 280 in the control simulation and perturbed with a range from 2.8 to 2800 (factor of 0.01 − 10 relative to the control value). The lower limit of the perturbation range is similar to the scaling factors in Sotiropoulou et al. (2020), considering that the original value from Takahashi et al. (1995) overestimates the number of fragments as their experiments were conducted with hails. Although the upper limit is highly unlikely for ice and snow particles due to the excessive number of fragments it implies, it was retained to ensure that the default value remains sufficiently distant from the boundary of the parameter space, where emulator predictions are generally associated with greater uncertainties. The multiple OAT test (Section 3.3) and global sensitivity analysis (Appendix G) were performed with the realistic range of E_{BR} from 2.8 to 280.

Compared to the parameterization from Phillips et al. (2017), which is based on collision kinetic energy, our approach here is simplified and only considered the broad type II of collision with graupel. Such choice was made to avoid extra complexity for parameter perturbation of the ice-ice collision process and future work is recommended to investigate with the parametrization from Phillips et al. (2017) for a more comprehensive understanding of the role of ice-ice breakup.

2.2.5 E_{DS} (efficiency of the droplet shattering process)

During the freezing of large supercooled droplets, the pressure inside the freezing droplets increases which can lead to the breakup of the frozen droplets and ice crystal formation (Leisner et al., 2014). Our approach follows the droplet shattering parameterization from Sullivan et al. (2018), in which the droplet shattering tendency is dependent on the number of fragments produced for each droplet shattering (E_{DS}), a temperature-dependent shattering probability (p_{DS}) and the Bigg droplet freezing rate (Bigg, 1953) (N_{Bigg}). The equation below shows the calculation of the number tendency of ice (N_{idps}) from the droplet shattering process. Details on p_{DS} can be found in Sullivan et al. (2018) and the Bigg droplet freezing in CASIM can be found in Field et al. (2023).

$$N_{\text{idps}} = (1 + p_{\text{DS}} E_{\text{DS}}) N_{\text{Bigg}} \tag{4}$$

The shattering probability was set to the same as the default one in Sullivan et al. (2018) with the shattering probability centred at -15 °C and the maximum probability set at 20%. E_{BR} was set to 5 in the control simulation with a perturbed range from 2 to 10 in the PPE design, following the sensitivity test values in Sullivan et al. (2018).

2.2.6 mpof (mixed-phase overlap factor)

When both ice and liquid clouds exist in the same model grid box, the mpof (mixed-phase overlap factor) is used for determining the extent to which ice and liquid co-exist in the same air in CASIM, which is important for mixed-phase processes (Field et al., 2023; Evans et al., 2025). We followed the naming of this parameter the same as in Field et al. (2023) and Evans et al. (2025) for consistency.

The mpof controls a function that quantifies the fractional overlap during the run time of the model rather than being a fixed value in a model grid box. When mpof is 1, the sub-grid liquid and ice cloud are maximally overlapped. When mpof is 0, the sub-grid liquid and ice are not overlapped as long as $CF_{\text{liq}} + CF_{\text{ice}} < 1$, where CF refers to cloud volume fraction
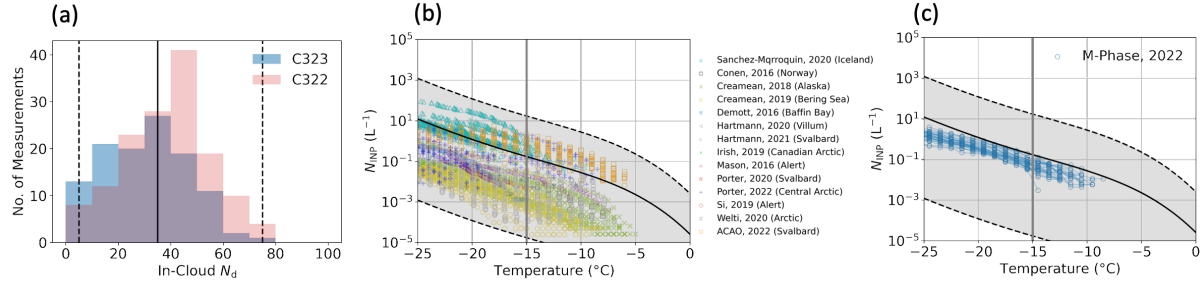
Figure 3. Comparison between the perturbed range and the measurements: (a) N_d with measured in-cloud N_d from M-Phase C322 and C323 using the CDP (cloud droplet probe) onboard; (b) perturbed temperature-dependent N_{INP} ranges compared to INP measurements at high latitudes in the Northern Hemisphere (Sanchez-Marroquin et al., 2020a; Franz Conen, 2016; Creamean et al., 2018, 2019; DeMott et al., 2016; Hartmann et al., 2020, 2021; Irish et al., 2019; Mason et al., 2016; Porter et al., 2020a, 2022; Si et al., 2019; Welti et al., 2020; Raif et al., 2024); (c) perturbed temperature-dependent N_{INP} ranges compared to all INP measurements from the M-Phase campaign (Tarn et al., 2025). Boundaries of each perturbed range (maximum and minimum values) are shown with dashed black lines, and the values used for the control simulations are shown with solid black lines. Cloud top temperatures are around -15 °C for the CAO clouds in this case and -15 °C is marked with bold gray solid line in (b) and (c).

in a model grid box. Once the combined cloud fraction goes above 1, there will be overlap. For an mpof of 0, the overlap is minimised. Values of mpof in between lead to increasing overlap, but once either the liquid or ice cloud fraction reaches 1, then

205 mixed-phase overlap is maximum whatever mpof is set to. See section A.6 in the documentation of CASIM implementation in the UM from Field et al. (2023) for more information. The mpof was set to 0.5 in the control simulation with a perturbed range from 0 to 1 in the PPE design.

2.2.7 Parameter design of PPE members

The maximin Latin hypercube sampling method was used to generate random combinations of parameter values across the

210 6-dimensional space for PPE simulations. The ranges of each parameter are discussed above. The maximin design maximizes the minimum distances between the points in parameter space. Each PPE contains 66 members following the guidance from Loeppky et al. (2009) that at least $10 \times n$ (where n is the number of parameters) simulations are required for training GP emulators. Two 6-member testing sets of simulations were also performed with parameter values from another maximin Latin hypercube sampling design. The testing simulations were used for assessing the performance of emulators trained with PPE

215 output. The values of parameters in the testing simulations were different from the ones in the PPE simulations which were used for training the emulators. Figure 4 shows the PPE and testing set input values.
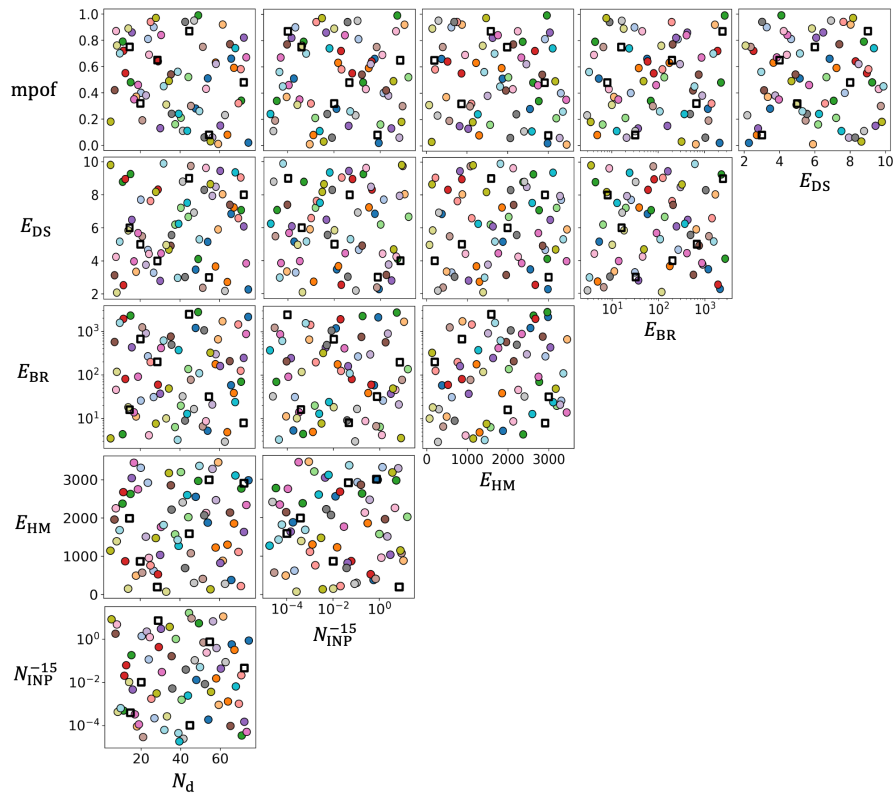
Figure 4. Paired combinations of parameters perturbed in this study. Colour filled circles are the 66 PPE members used for training the GP emulators, and the unfilled squares are the six testing members used for testing the trained GP emulators. Each colour suggests a set of parameter values. Results of kernel selection, validation and testing are shown in Appendix C.

2.3 Gaussian Process (GP) emulators

Gaussian Process (GP) emulation is a non-parametric supervised machine learning method that learns the relationship between model input parameters and outputs of interest (Oakley and O'Hagan, 2002; O'Hagan, 2006). GP emulators were constructed

220 on the output from the PPE simulations and acted as a statistical "surrogate" model for the computationally-expensive numerical model. The GP emulators enabled efficient exploration of the entire parameter space with dense sampling, allowing for construction of multi-dimensional response surfaces and a variance-based sensitivity analysis to assess the importance of the perturbed parameters to the cloud variables. Detailed methodologies and explanations on building GP emulators for climate and atmospheric models can be found in Lee et al. (2011) and Johnson et al. (2015).

225 A GP emulator consists of a mean function and a covariance function, also called the kernel. To obtain a good GP emulator of each variable of interest we tested four commonly-used stationary kernels: the Radial Basis Function (RBF) kernel and three Matérn kernels with different smoothness parameters: the Matérn12 kernel (0.5), the Matérn32 kernel (1.5) and the Matérn52 kernel (2.5), implemented in the GP Jax Python library for Gaussian processes (Pinder and Dodd, 2022). When the smoothness parameter becomes infinite in a Matérn kernel, it becomes equivalent to the RBF kernel. For each variable, we

230 conducted cross-validation by dividing the 66 PPE members into 11 sets with 60 training and 6 validation data points per set. The cross-validation was used here to maximise the use of our limited data due to the high computational cost of running the numerical simulations. Emulator performance was assessed with graphical diagnostics including individual standardized error plots and Q-Q plots following the guidance from Bastos and O'Hagan (2009), as well as the RMSE (root mean squared error) and R^2 (coefficient of determination). The kernel selection was mainly based on the RMSE values, with the Q-Q plots and

235 R^2 for supporting the assessment. Once the best-performing kernel was selected for each variable, we trained the GP emulator with the best kernel on all 66 PPE members and tested it with the corresponding testing set. Appendix C shows the emulator performances from the kernel selection and testing steps.

3 Results

3.1 Example response from PPE simulations: TOA albedo

240 Before analysing emulated response surfaces of domain-mean outputs in the next section, we first illustrate the strength of
perturbing parameters in a PPE design and use TOA albedo here as an example in Figure 5. Note that the emulators (Section 3.2)
define the relationship between input parameters and mean output variables (e.g., domain-mean albedo) and cannot describe
the specific cloud patterns shown here, hence why we start by showing the results of some PPE members. We selected two
parameters to demonstrate the PPE results: N_d and N_INP^{-15} for the Sc region, and N_d and mpof for the Cu region. These parameter

245 pairs were chosen only for illustration because, as we show in Section 3.2, they have the strongest joint effects on cloud albedo
in each region.

Figure 5 shows the maps of TOA albedo in 25 of the 66 PPE simulations over the two regions. The intervals between each
PPE output are not equal in Figure 5 because of the Latin hypercube design method used for sampling the parameter space,
and the subplots shown in Figure 5 are only ordered using the values of the selected parameters with the values of other four

250 parameters ignored.

In both regions, the selected parameters jointly affect the TOA albedo. For example, in the Sc region (Figure 5a), low
N_d and high N_INP^{-15} (top left subplot) result in the lowest TOA albedo, while high N_d and low N_INP^{-15} (bottom right subplot)
result in the highest TOA albedo. With PPE simulations, we can see clear joint effects of parameters on cloud properties.
However, the number of simulations is too small to identify whether the joint effects are linear (combined effects) that could

255 be predicted from combinations of OAT simulations, or non-linear (interactive effects) (Sansom, 2023). See Appendix E for a
simple illustration of linear and non-linear joint effects between two parameters. Using the emulators enables a much denser
sampling of the parameter space and, as we show in Section 3.2, exposure of non-linear effects (interactions) of combinations
of parameters that are not apparent in Figure 5.
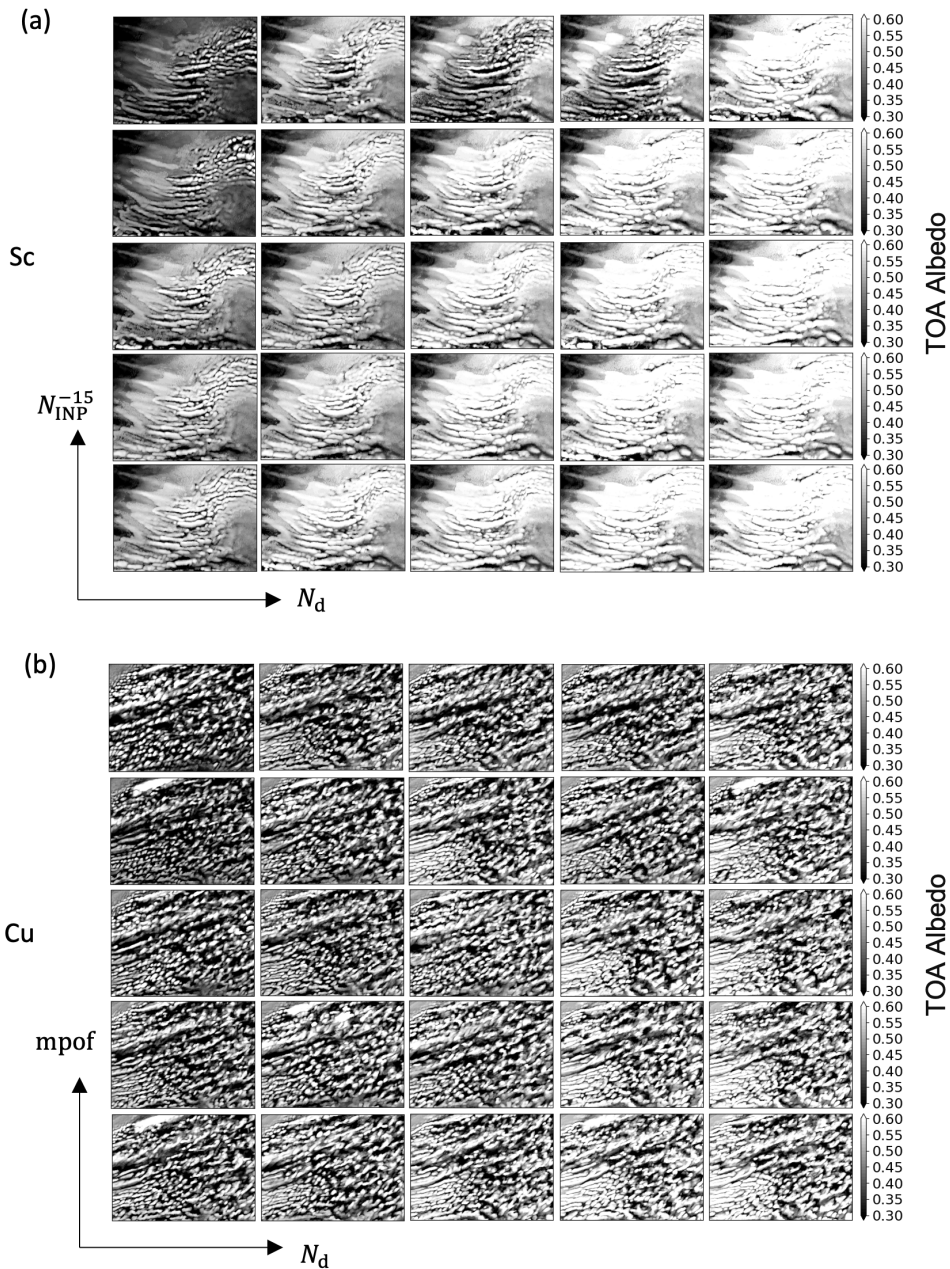
Figure 5. Responses of TOA albedo for maps of (a) the Sc region ordered according to N_d and N_INP^{-15} and (b) the Cu region ordered according to N_d and mpof. The selected model output time is 16:00 UTC. The selected domains are the same as the regions shown in Figure 1. Note that each image shows a different simulation, and only 25 out of the 66 PPE parameters are shown here. Because of the Latin hypercube design method used for sampling the parameter space, the subplots shown here are only ordered using the values of the selected two parameters with the values of other four parameters ignored and the intervals between of these subplots for each parameter are not the same.

3.2 Emulated model response surface

260 The PPE members provide considerable information about cloud behaviour across the 6-D parameter space, but the data sparseness (just 66 points in 6-D space) limits our ability to visualise joint parameter effects or to perform statistical analysis. Therefore, we built emulators of temporally and spatially averaged cloud properties, which enable 6-D continuous response surfaces to be created. The time of averaging is from 12 UTC to 19 UTC, and the domains of averaging are shown as analysis domains in Figure 1. The response surfaces were generated by predicting one million output values from the emulators across

265 the parameter space.

Figure 6 shows the distributions of TOA albedo, cloud cover, all-sky LWP (liquid water path), all-sky IWP (ice water path) and all-sky TWP (total water path) from one million combinations of parameters drawn from the GP emulators. By perturbing all 6 parameters in the Sc region, the TOA albedo ranges from 0.43 to 0.54 (inter-percentile range from 5% to 95%), cloud cover from 0.84 to 0.91, LWP from $74.5\,\mathrm{g\,m^{-2}}$ to $149.5\,\mathrm{g\,m^{-2}}$, IWP from $0.0\,\mathrm{g\,m^{-2}}$ to $38.1\,\mathrm{g\,m^{-2}}$ and TWP from $97.6\,\mathrm{g\,m^{-2}}$

270 to $148.4\,\mathrm{g\,m^{-2}}$. In the Cu region, the TOA albedo ranges from 0.37 to 0.44, cloud cover from 0.78 to 0.84, LWP from 47.9 $\mathrm{g\,m^{-2}}$ to $98.4\,\mathrm{g\,m^{-2}}$, IWP from $71.3\,\mathrm{g\,m^{-2}}$ to $186.1\,\mathrm{g\,m^{-2}}$ and TWP from $147.8\,\mathrm{g\,m^{-2}}$ to $244.4\,\mathrm{g\,m^{-2}}$.

Figures 7 and 8 show the joint effects of each combination of two parameters with the other parameter effects averaged for TOA albedo and all-sky LWP, which are two key properties for cloud-phase feedback, respectively over the two selected regions. These are known as "paired projections". Paired projections for cloud cover, all-sky IWP and all-sky TWP are shown

275 in Appendix F. The values shown on the paired projection plots are calculated by averaging over the other four dimensions, and therefore describe the mean response of each variable to each paired parameter set.

Using the paired-projections, we are able to qualitatively identify key parameters controlling the cloud properties over the parameter space. In the Sc region, N_d and N_INP^{-15} exert the strongest effects on TOA albedo and LWP. All parameters from SIP processes and mpof only show weak effects across the projections due to the liquid-dominated nature of these clouds,

280 demonstrating limited effects in the Sc region. In the Cu region, N_d maintains its strong influence on TOA albedo and LWP, while the second most strongest effect is now from varying mpof. The perturbation of mpof now results in a stronger effect on cloud properties compared to in the Sc region and to N_INP^{-15} in the Cu region. A reduction in mpof leads to less interactions of liquid and ice particles, which weakens the removal of liquid water through accretion. The increasing effect from mpof in Cu region than the Sc region comes from an increasing ice formation in Cu clouds when the cloud top deepens and more mixing

285 between ice and liquid hydrometeors.

All three SIP parameters have a relatively weak effect on TOA albedo and LWP in both Sc and Cu regions, even though the cloud temperature covers most of the active temperature range of the HM process. Note that a low sensitivity does not imply that SIP is unimportant, only that the cloud properties are fairly insensitive to its precise value. Although the influences from varying SIP processes on albedo and LWP are small in both regions, the effect of each parameter is specific to this case study

290 and is not representative of all mixed-phase CAO clouds. The HM process has a much stronger effect on IWP and TWP in the Cu region (Appendix F), but such influence is weakly transferred to the radiative properties (TOA albedo).

The influences of N_{INP}^{-15} and mpof on TOA albedo are weaker compared to their influences on LWP in both regions. This is because perturbing N_{d} also changes the single scattering albedo of cloud droplets and exerts a strong Twomey effect on the liquid-dominated Sc clouds (over 80% of the Sc cloud water mass is liquid in the control simulation). As a result, the

295   effect of perturbing N_{INP}^{-15} and mpof on TOA albedo become smaller than their effects on LWP. There are also non-monotonic responses of LWP to the perturbation of N_{INP}^{-15} at lower N_{INP}^{-15} values in the Sc region. An increase in N_{INP}^{-15} does not lead to a monotonic decrease in LWP; instead, LWP initially increases with increasing N_{INP}^{-15}, followed by a decrease at higher N_{INP}^{-15}. This may because the removal of liquid through warm rain processes is first reduced when increasing N_{INP}^{-15} as the amount of liquid is reduced, hence leading to a higher LWP; but with further increases in INPs, the removal of liquid is then dominated

300   by the mixed-phase processes rather than the warm rain processes, hence leading to a lower LWP eventually. One can also see that, as N_{d} increases, the warm rain processes reduce due to less rain autoconversion, and the value of N_{INP}^{-15} required to let mixed-phase processes start dominating the water removal process (where the increasing LWP becomes decreasing LWP with increases in INP) decreases. To further test this, one can compare different model response surfaces between N_{d} and N_{INP}^{-15} with and without the warm rain and cold rain processes.

305   For most of the paired projections, non-linear joint effects (interactions) of the parameters on the cloud properties can be identified. Here we use the projections between N_{d} and N_{INP}^{-15} in the Sc region and the ones between N_{d} and mpof in the Cu region as examples. Parameter interactions are apparent when the sensitivity of a cloud property to a parameter perturbation depends on the value of another parameter - i.e., the number of contours across for the same change of a parameter differs when the value of another parameter changes. Using LWP in the Sc region as an example, by perturbing N_{d} from low to high

310   values and keeping N_{INP}^{-15} low (less than 0.01 L^{-1}), the LWP ranges from approximately 90 $\mathrm{g\,m}^{-2}$ to 140 $\mathrm{g\,m}^{-2}$; if the N_{INP}^{-15} is high (more than 1 L^{-1}), the LWP range approximately from 70 $\mathrm{g\,m}^{-2}$ to 95 $\mathrm{g\,m}^{-2}$. In the Cu region, the LWP ranges from 70 $\mathrm{g\,m}^{-2}$ to 90 $\mathrm{g\,m}^{-2}$ for low to high N_{d} values when mpof is low (less than 0.2), but from 50 $\mathrm{g\,m}^{-2}$ to 60 $\mathrm{g\,m}^{-2}$ when mpof is high (more than 0.6).

Another example of parameter interactions is that the local sensitivity of a parameter can vary across the parameter space.

315   In the Sc region, the LWP is insensitive to N_{INP}^{-15} when N_{d} is lower than approximately 20 cm^{-3} and N_{INP}^{-15} less than 0.1 L^{-1}, while it becomes very sensitive to N_{INP}^{-15} when N_{d} is higher than approximately 50 cm^{-3}. The relative importances of SIP processes and mpof in the Sc region also depend on the values of N_{d} and N_{INP}^{-15}, despite the perturbations of SIP parameters and mpof having limited effect on cloud radiative properties in this region. When N_{d} is higher than about 40 cm^{-3} or N_{INP}^{-15} lower than 0.01 L^{-1}, the influence on LWP is strongly enhanced by SIP processes and mpof. It is worth noting that the effects

320   of SIP processes and mpof on LWP are still quite small, so although they strongly affect the change in LWP in that part of the parameter space, their importance over the whole parameter space is small compared to N_{d} and N_{INP}^{-15}. Such interdependency between the parameters shows that a single OAT test is insufficient to draw conclusions about the importance of a parameter or a process, and the results from the OAT test are highly dependent on the default values of the parameters in the control simulation.

325   Figures 6-8 also show that different combinations of parameter values may result in the same value of cloud properties, which is called equifinality (Beven, 2006; Lee et al., 2016; Carslaw et al., 2025). For example, the mode TOA albedo in
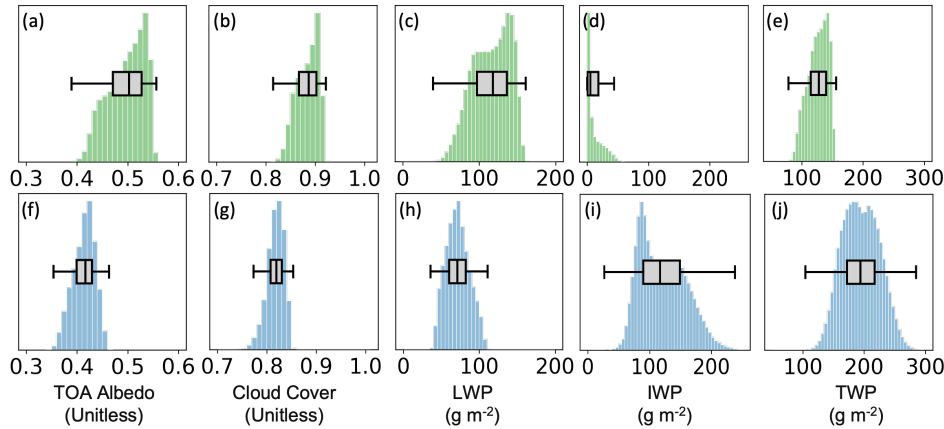
Figure 6. Distributions of cloud variables from 1 million combinations of parameter values for (a) all-sky TOA albedo (unitless), (b) cloud cover (unitless), (c) all-sky LWP $(\mathrm{g\,m^{-2}})$; (d) all-sky IWP $(\mathrm{g\,m^{-2}})$ and (e) TWP $(\mathrm{g\,m^{-2}})$ which is the sum of LWP and IWP. Separate distributions are shown for the Sc (top row) and Cu (bottom row) regions.

the Sc region is 0.54, meaning a large number of model variants with different parameter values produce the same albedo of 0.54. The equifinality is also visible in the filled contour plots in the paired projections shown in Figures 7 and 8 - each contour colour defines parameter combinations that produce equifinal model output. Equifinality becomes important when
330 model output is compared to observations, because model output from different combinations of parameters will agree equally well with observations. Perturbing each parameter individually to match observations may fall into the problem of equifinality because it would result in a single and overly confident estimate of a parameter value rather than a range. Here we use TOA albedo as an example. The observed, domain-mean TOA albedo from CERES onboard the Aqua satellite is around 0.48 in the Sc region and around 0.39 for the Cu region at 17:00 UTC. There are more than 70,000 model variants out of the 1 million
335 model variants that produce this value of TOA albedo (+/- 0.005) in the Sc region, and more than 90,000 model variants in the Cu region. There would also be many more equifinal variants when accounting for observation uncertainty. Such equifinality problem suggests that using a single variable to constrain the parameter space is not sufficient, and multiple variables for different cloud properties are needed. A key question is whether there exists a single part of parameter space for which all the variables agree well with observations, which will be shown in our subsequent paper comparing the PPE simulations shown in
340 this work with multiple observations (*in-situ* and satellite).
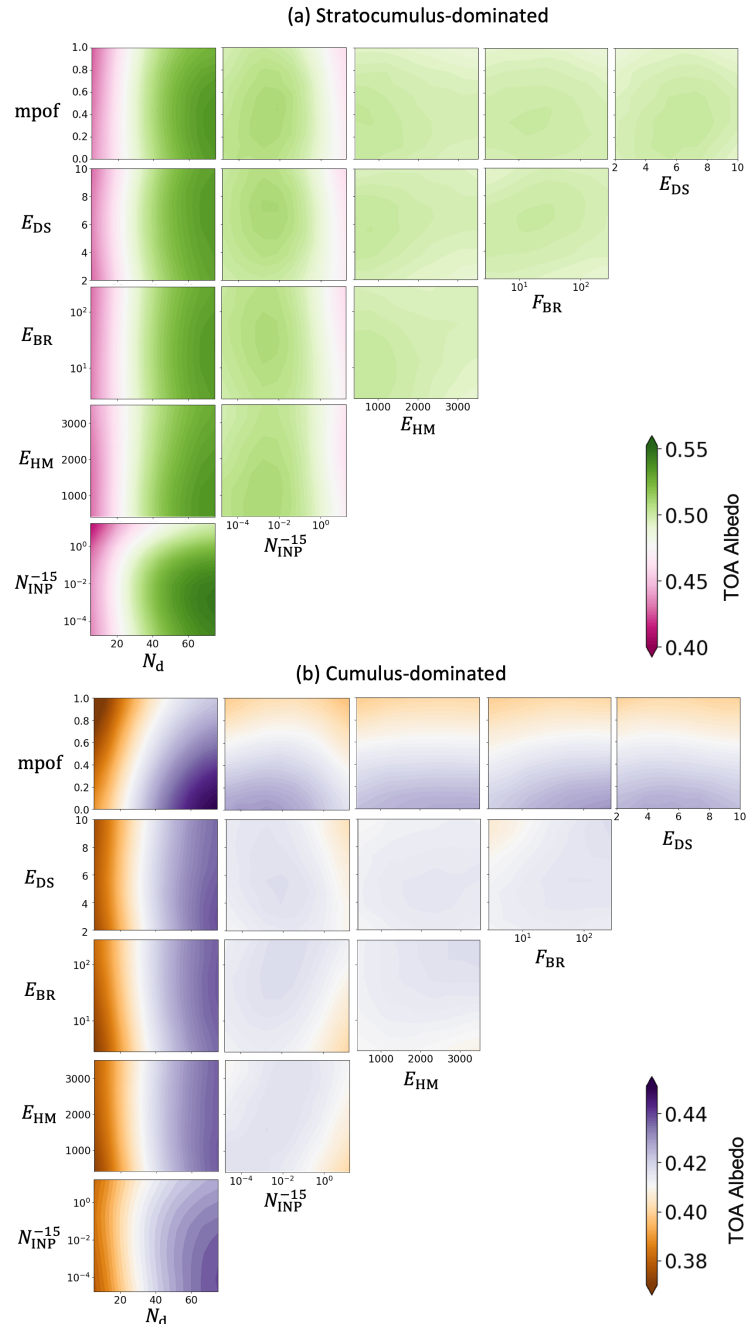
Figure 7. Emulated mean model responses of all-sky TOA albedo to paired parameters in (a) the Sc region and (b) the Cu region. The values shown on the paired projection plots are calculated by averaging over the other four dimensions, and therefore describe the mean response of each variable to each paired parameter set.
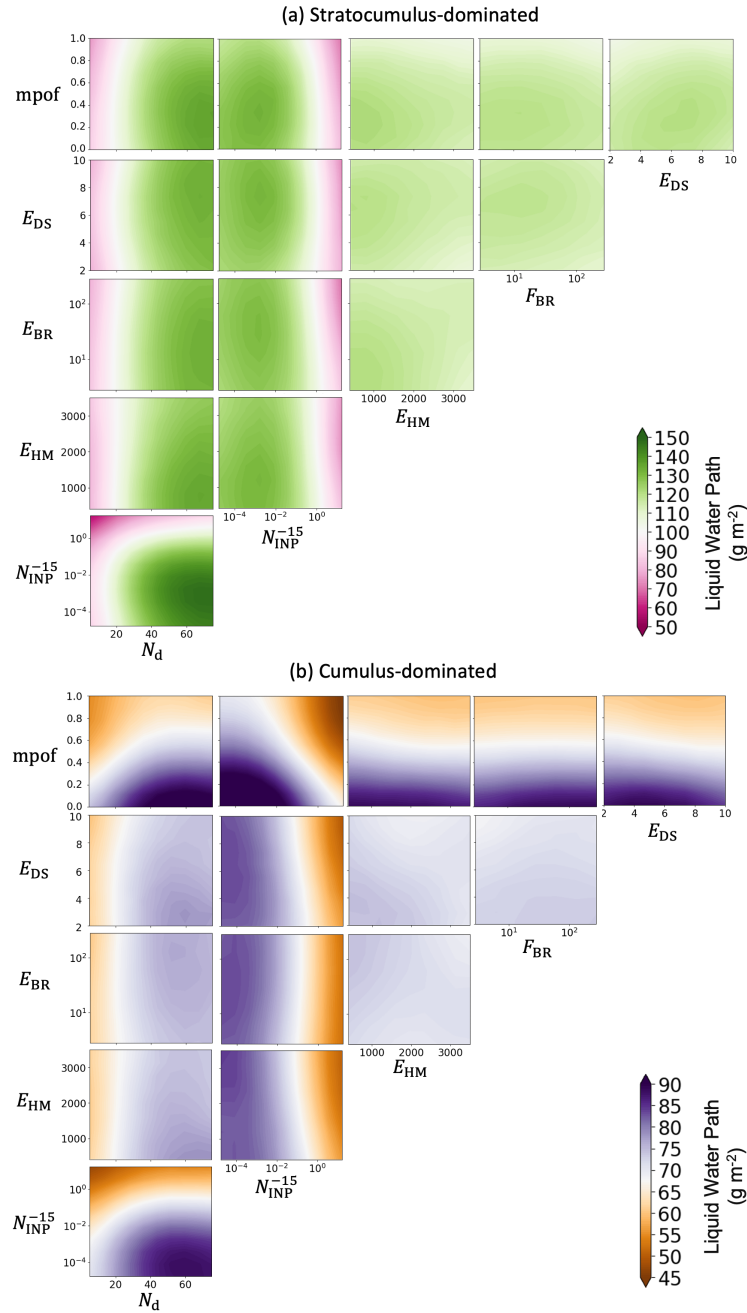
Figure 8. Emulated mean model responses of all-sky LWP to paired parameters in (a) the Sc region and (b) the Cu region. The values shown on the paired projection plots are calculated by averaging over the other four dimensions, and therefore describe the mean response of each variable to each paired parameter set.

3.3 Dependence of individual parameter sensitivities on other parameters

The response surfaces shown in the previous section show that the sensitivity of cloud properties to a change in a parameter depends strongly on the setting of the other parameters. However, these paired projections neglect variations in the other four parameters and therefore only present the mean response of each model variable to each paired parameter set. Therefore, to understand how much the sensitivities of cloud properties vary within the parameter space, we present the results from multiple OAT tests across the parameter space in Figure 9.

We performed a large number OAT tests using the trained GP emulators for each model variable with different starting points. To design the starting points, three values were selected for each parameter: low (25% of the perturbed range), mid (50% of the perturbed range), and high (75% of the perturbed range). For N parameters each with M values, the number of possible parameter combinations are M^N. Hence, there were 729 starting points (control sets of parameter values) across the 6-D parameter space in the multiple OAT tests. For each OAT test, the parameters were perturbed to the high-end (95% of the perturbed range) and the low-end (5% of the perturbed range) individually. The responses of cloud properties were the change from high-end parameter value output to the low-end parameter value output. The perturbed ranges in the multiple OAT tests were smaller than the parameter range in the PPE design to avoid the high uncertainties of emulators near boundaries of the parameter space. As for each parameter, we perturbed the value from low-end to high-end without directly including the emulator output from the control simulation, the number of output points from the emulator for each variable is $2 \times M^{N-1}$. Therefore, for each model variable in one domain (one subplot in Figure 9), the total number of investigated model variants is 2916. A compact distribution in Figure 9 means that the sensitivity of the cloud property to that parameter is not strongly dependent on the setting of the other parameters.

The magnitudes of cloud responses to individual parameter perturbations are sometimes strongly dependent on the values of other parameters. For example, in the Sc region, the increase in LWP (Figure 9e) by perturbing N_{d} from low to high values ranges from +31 $\mathrm{g\,m^{-2}}$ to +65 $\mathrm{g\,m^{-2}}$, and the decrease in LWP by perturbing N_{INP}^{-15} from low to high values ranges from -73 $\mathrm{g\,m^{-2}}$ to -29 $\mathrm{g\,m^{-2}}$. In the Cu region, the decrease in LWP (Figure 9f) by perturbing mpof from low to high values ranges from -39 $\mathrm{g\,m^{-2}}$ to -15 $\mathrm{g\,m^{-2}}$. Although the projection plots suggest clouds are not very sensitive to variations of SIP processes, the multiple OAT tests here show that in some parameter space, varying SIP processes can have same or even stronger effects on cloud cover, IWP and TWP in the Cu region than N_{d} and N_{INP}^{-15}. In addition, due to the existence of dominant parameters across the parameter space (e.g., N_{d}), the effects from SIP processes may be obscured through averaging in the paired projections. The relative importance of each parameter across the parameter space can also be quantitively compared by using the statistics of the sensitivities from the multiple OAT test (e.g. mean or mode), which shows similar results to those from a global sensitivity analysis in Appendix G.

The direction (or sign) of the cloud response can also depend on the control values of the parameters. For example, changes in SIP parameters can cause either increases or decreases in cloud cover (Figures 9c and 9d) depending on the other parameters (primarily N_{d} and N_{INP}^{-15} which dominate the sensitivities). In the Cu region, increasing N_{INP}^{-15} does not consistently lead to a reduction of the TOA albedo (Figure 9b). For most OAT tests with N_{INP}^{-15} perturbations, increasing N_{INP}^{-15} causes cloud cover to

375   increase (Figure 9d), but also leads to a reduction in LWP (Figure 9f). These two effects compensate each other for the effect of increasing N_{INP}^{-15} on TOA albedo. Therefore, the influence from a high N_{INP}^{-15} on TOA albedo in Cu region is controlled by multiple cloud properties, and these cloud properties can have different responses to changing N_{INP}^{-15} at different part of the parameter space.

    In summary, the sensitivities of modelled cloud properties to each individual perturbed parameter depend on the starting

380   point in the parameter space; this includes both the magnitudes and sign of responses. Results from our multiple OAT tests across the parameter space demonstrate that using a single OAT test is inadequate for determining the magnitude and even sign of the cloud response to model parameters. It is therefore important to investigate the whole parameter space for a more comprehensive understanding of the effects from these parameters.
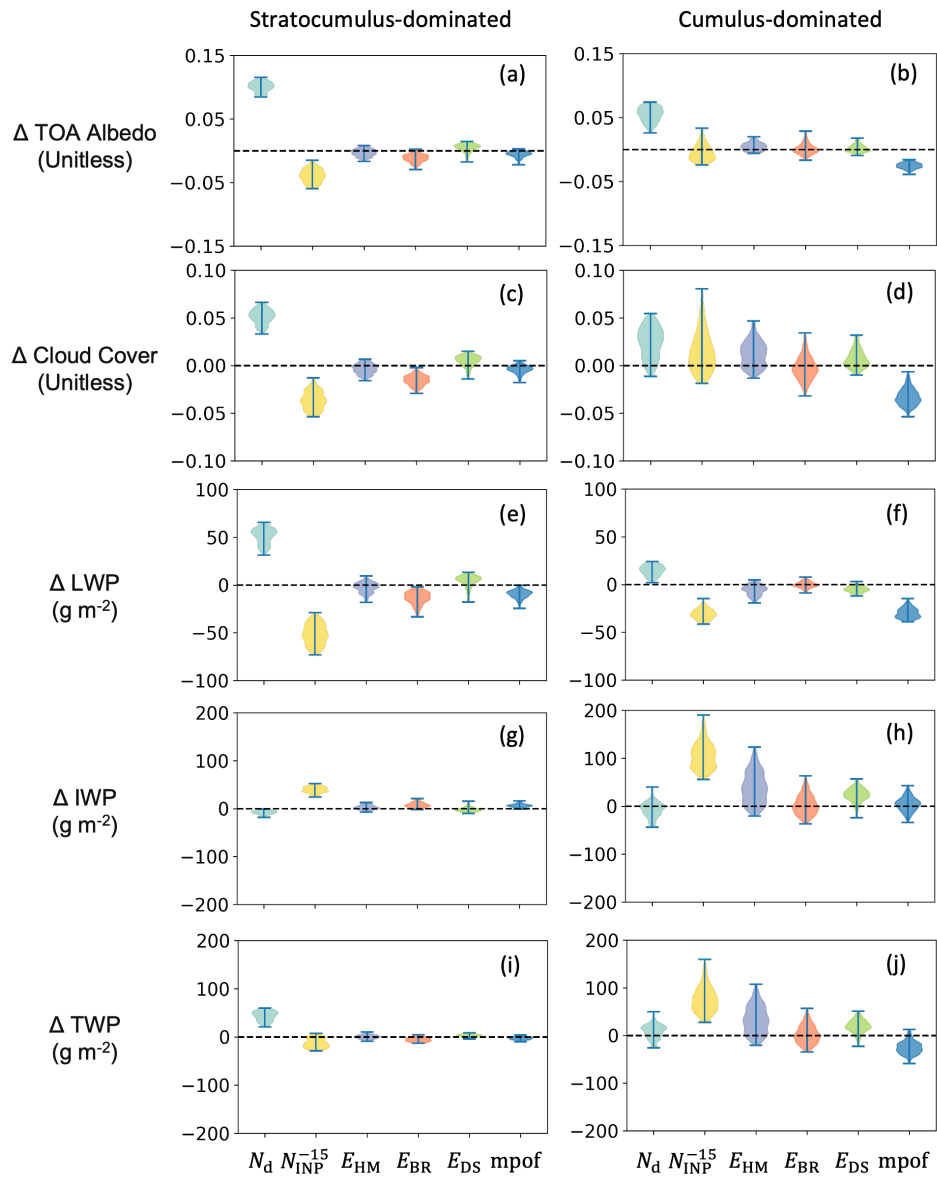
Figure 9. Distributions of the cloud property changes resulting from an increase of individual parameters one-at-a-time (OAT) in multiple OAT tests for: all-sky TOA albedo (a, b), cloud cover (c, d), all-sky LWP (e, f), all-sky IWP (g, h), and all-sky TWP (i, j). The left panel shows the results from the Sc region, and the right panel shows the results from the Cu region. Errors of the GP model are propagated through into these multiple OAT test results, but the errors are generally much smaller than the variations shown here (Appendix C). For the process of performing the multiple OAT test, please refer to the details in Section 3.3.

4 Discussion and Conclusions

385 We present here the first analysis of mixed-phase CAO (cold-air outbreak) cloud responses to combinations of six key cloud microphysics parameters related to aerosol-cloud interactions and ice formation processes. The perturbed ranges of these parameters either match the observed ranges when available, or were chosen based on uncertain ranges suggested by previous studies. The full 6-dimensional parameter space of cloud responses was explored using PPEs (perturbed parameter ensembles), GP (Gaussian Process) emulators, and multiple OAT (one-at-a-time) tests across the whole parameter space. The properties we

390 investigated included all-sky TOA (top-of-the-atmosphere) albedo, all-sky LWP (liquid water path), cloud cover, all-sky IWP (ice water path) and all-sky TWP (total water path) which are key properties that influence the radiative effects of mixed-phase clouds (Ceppi et al., 2017). Model simulations were based on a CAO event case over the Labrador Sea on 24 October 2024, focused on Sc(stratocumulus) and Cu(cumulus) cloud regimes and covering the routes of two research flights from the M-Phase aircraft campaign (Murray and the M-Phase Team, 2024; Clarke et al., 2025).

395 In this CAO case, where the liquid phase dominates with cloud top temperatures of around -15 °C, N_d exerts the strongest controls on TOA albedo and LWP in both regions with the Twomey effect (Twomey, 1977) and the Albrecht effect (Albrecht, 1989). The effects of N_d on mixed-phase CAO clouds in these simulations are also consistent with previous simulations from de Roode et al. (2019) who reported that higher N_d leads to a higher LWP and cloud cover, and vice versa. However, we further show that the effect of changing N_d varies strongly across the parameter space. Perturbing N_d from low to high in different

400 parts of the parameter space leads to TOA albedo responses ranging from +0.08 to +0.11 and LWP responses ranging from +31 $\mathrm{g\,m^{-2}}$ to +65 $\mathrm{g\,m^{-2}}$ in the Sc region, and TOA albedo responses ranging from +0.02 to +0.07 and LWP responses ranging from near-zero (+2 $\mathrm{g\,m^{-2}}$) to +24 $\mathrm{g\,m^{-2}}$ in the Cu region. Thus, although the effect of N_d on albedo and LWP are dominating, there are strong variations depending on other parameters. Such variation demonstrates the importance of performing simulations across a joint parameter space to avoid incomplete conclusions or overly confident estimates of sensitivities.

405 An increase in N_INP^{-15} leads to a reduction in TOA albedo and LWP in the Sc region, which is consistent with the results from previous studies on the influences of different INP concentrations (Tornow et al., 2021) or ice treatment in models (Abel et al., 2017). However, the sampling of parameter space using PPEs and emulators shows that the magnitude and even sign of response to N_INP^{-15} perturbations depends on the setting of other parameters, even within the single environment represented by the case we studied. It is seen in the Sc region that the modelled TOA albedo is not sensitive to N_INP^{-15} when N_d is low

410 (less than approximately 20 $\mathrm{cm^{-3}}$). A similar weak sensitivity of clouds to changes in N_INP^{-15} was found by the study from McCluskey et al. (2024) over the Southern Ocean, where they found that the modelled IWP was relatively insensitive to the representation of INP under low N_d condition. It is shown that their model underestimate CCN concentration (Niu et al., 2025) over the Southern Ocean, which could account for the weak INP sensitivity consistent with our results. We also find that in the Cu region, the sensitivity of clouds to N_INP^{-15} is relatively weaker and the sign of the cloud response as a function of N_INP^{-15}

415 varies over the parameter space. For example, an increase in N_INP^{-15} can lead to both increases and decreases of TOA albedo (from -0.02 to +0.03) and cloud cover (from -0.02 to +0.08) when the values of other parameters are changed. The pronounced variation in the modelled cloud sensitivity to INP concentrations highlights the importance of having good representations of

22

other microphysical processes in the model and the necessity of a full exploration of the parameter space, including other cases, to understand the role of INPs in mixed-phase CAO clouds.

420   Our results results show that aerosols (which affect N_d and N_{INP}^{-15}) strongly control mixed-phase cloud radiative properties in the Sc region, but with large uncertainty in the sensitivities depending on other poorly quantified model parameters. Observational constraints can be obtained from satellite retrievals and applied to constrain the N_d part of the parameter space, but measurements of N_{INP} are sparse and difficult to be obtained from satellite, leaving the sensitivity of clouds to N_{INP} difficult to constrain. A high temporal and spatial coverage of INP measurements are therefore needed to constrain the properties and

425   sensitivities of mixed-phase CAO clouds.

     The SIP parameters generally have a weak effect on the radiative properties (TOA albedo) of CAO clouds in this case. Our results on the effect from SIP processes on LWP are generally consistent with previous work from Karalis et al. (2022) who showed that an enhancement of SIP can lead to the reduction of LWP. However, we show that the magnitude of LWP (and other cloud properties) responses to perturbations of all three SIP parameters vary across the parameter space, with strong

430   dependency on the other parameters such as N_d and N_{INP}^{-15}. Compared to the results from Karalis et al. (2022), the relative importance of each of the SIP process differs between our study and theirs. In Karalis et al. (2022), the droplet shattering process was more effective than the Hallett-Mossop process in the Cu region, while the Hallett-Mossop process exerts stronger effects on LWP in our case. Such differences may occur because the environmental conditions vary between cases, which will affect the efficiencies of SIP processes. In addition, Karalis et al. (2022) used alternative parameterizations for the droplet-

435   shattering and ice-ice break processes which follow Phillips et al. (2017). Therefore, it is worth noting that our conclusions are potentially specific to this CAO case and may be dependent on the CAO case being simulated, and may be influenced by the model setup or choice of parameterizations.

     The influence of mpof is more prominent in the Cu region where an increase in mpof leads to a reduction in LWP and cloud cover, and therefore a lower TOA albedo. These responses of cloud properties to changes in the mpof value are similar to the

440   results from Abel et al. (2017). However, the sensitivity of LWP as a function of mpof in our work is weaker in the Sc region than seen in Abel et al. (2017) where they also modified the cloud liquid and ice overlap. Although our case here has similar cloud temperature as the case investigated in Abel et al. (2017), the overlap parameter used in their work is from the bulk cloud scheme, while the mpof in our work is within the cloud microphysics scheme. This suggests that different model setups can also lead to potentially different sensitivities of cloud properties to the parameters. Similar to the other parameters, the effect

445   from mpof on the investigated cloud properties vary across the parameter space and interactively affect the influence of the other parameters.

     We expect the large, non-linear joint effects of cloud microphysical parameters on CAO clouds will be a feature of CAOs in other meteorological environments, but the sensitivities are likely to vary. By limiting our analysis to a single case study, we are able to fully explore the sensitivity of the CAO clouds to six key parameters without the confounding effects of environmental

450   conditions. The sensitivity of mixed-phase CAO clouds to the parameters investigated here may be substantially different in a different CAO event, as we have shown in previous work by comparing the responses from warm and cold CAO cases (Huang et al., 2025). We also made some simplifications to the cloud microphysics processes (e.g. no spatial variation of N_d and N_{INP})

and did not include all important parameters and processes such as boundary layer mixing (Field et al., 2014) and cloud fraction schemes (cloud macrophysics) (Van Weverberg et al., 2023), for the reason to enhance the interpretation of the complex model output. Future work is recommended to investigate the control of various environmental conditions on CAO clouds and their interactions with key cloud parameters. It is also recommended to include aerosol processes for a complete understanding of aerosol influences on mixed-phase CAO clouds.

To conclude, this work illustrates the power of using PPEs and model emulation for systematically quantifying important non-linear joint effects of multiple cloud microphysical parameters on mixed-phase CAO clouds. These interactions of parameters cannot be revealed using single OAT tests, which may therefore lead to misleading or overly confident estimates of the key factors controlling mixed-phase cloud properties. Exploration of the entire parameter space is necessary to fully understand the influences on CAO clouds from these uncertain model parameters, and to constrain the effect of the uncertainties on the estimation of cloud-phase feedback.

Data availability. MODIS Level 1B Calibrated Radiances Product (Collection 6.1) onboard the Aqua satellite for RGB composites with bands 1,3 and 4 were obtained from https://ladsweb.modaps.eosdis.nasa.gov/missions-and-measurements/products/MYD021KM with geolocation data from https://ladsweb.modaps.eosdis.nasa.gov/missions-and-measurements/products/MYD03. The INP data during the M-Phase aircraft campaign were obtained from https://zenodo.org/records/14781199.The measurements during the M-Phase aircraft campaign can be obtained from https://catalogue.ceda.ac.uk/uuid/7569dbd04216467db6fc2529a7bc2a6f for M-Phase C322 and https://catalogue.ceda.ac.uk/uuid/586d4691756c4a91b5ad2d0b14bf10c7 for M-Phase C323. Processed data from PPE simulations for both regions can be obtained from https://doi.org/10.5281/zenodo.18267702.

Appendix A: Deriving a new $n_s(T)$ parameterization for soil dusts

A recent study by Herbert et al. (2025) has shown that the ice-nucleating ability of dust in the atmosphere is influenced by a mineral component and a biogenic component associated with the surface area of the dust. The authors suggest that soil dusts that have come from arid, desert-like, environments are best represented by the mineral component alone, whereas dusts

475   from biologically productive regions are best represented by the inclusion of both components. The authors refer to these two classes of soil dusts as *desert soils* and *fertile soils*, respectively. Some parameterizations that are commonly used to represent INP concentrations in modelling studies (Harrison et al., 2019, e.g.,) only account for the mineral component, and therefore may only be representative of desert soils. Here, we present a new empirical parameterization for the ice-nucleating activity of fertile soils, which is likely more representative of INP measurements in the mid- to high latitudes (Herbert et al., 2025).

480   Laboratory measurements of soil-dust ice nucleating activities were collated from literature (Barr et al., 2023; King, 2024; O'Sullivan et al., 2014; Paramonov et al., 2018; Porter et al., 2020b; Sanchez-Marroquin et al., 2020b; Steinke et al., 2020; Thompson, 2024; Steinke et al., 2016). These are studies that have tested the untreated properties of soil dusts that have been sampled in situ or collected from the surface. We purposefully omit measurements from desert soil sources, such as the Sahara desert.
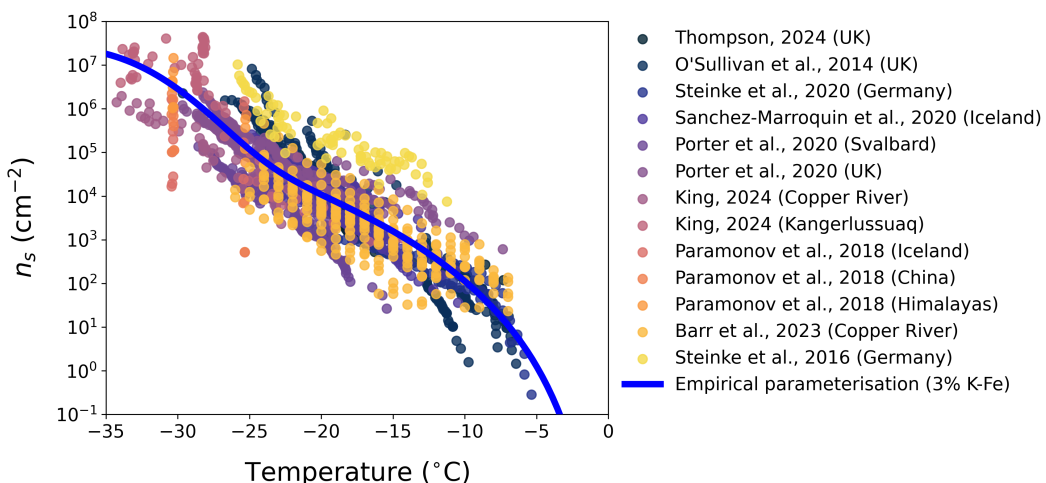
Figure A1. Empirical soil-dust parameterization of $n_{s,\text{soil}}(T)$. Coloured circles show measurements from laboratory studies (references within figure) that have measured the ice-nucleating activity of soil dust sampled from locations around the world. The solid blue line shows the best fit to the data assuming a K-Fe component (weight percent of 3 %) and a biogenic component described by a power law.

485   We use the measurements to produce an empirical parameterization which consists of two additive functions, accounting for the two components. For the mineral component, we use a parameterization from Harrison et al. (2019) that is dependent on the potassium-feldspar (K-Fe) present in the dust. We use a constant K-Fe content (f_{KFe}) of 0.03, which is representative of a global-mean value (Harrison et al., 2019). For the biogenic component, we use the power law $n_s(T) = -kT^\alpha$, which provides

Table A1. Polynomial coefficients used in Eq. A1. Values are taken from Harrison et al. (2019)

Polynomial coefficient	Value
P_1	-3.25
P_2	-0.793
P_3	-6.91×10^{-2}
P_4	-4.17×10^{-3}
P_5	-1.05×10^{-4}
P_6	-9.08×10^{-7}

a shape consistent with measurements of n_s at high temperatures (Figure A1). The variables α and k were systematically varied

490   until the root-mean square error between the measurements and summed contributions of the two functions was minimized. The resulting parameterization of $n_{s,\mathrm{soil}}(T)$ in cm^{-2} is shown in Figure A1, and described by the function

$$n_{s,\mathrm{soil}}(T) = (-kT^{\alpha}) + 10^{(P_1+P_2T+P_3T^2+P_4T^3+P_5T^4+P_6T^5)} f_{\mathrm{KFe}}, \tag{A1}$$

where $k = 3.907 \times 10^{-5}$, $\alpha = 6.531$, and the values of P_1 to P_6 are shown in Table A1. The temperature T is in °C.

Appendix B: Simulated dust size distributions during M-Phase

495   In this section, we produce an INP parameterization that is representative of the location and time period of the M-Phase campaign. We apply the new $n_{s,\text{soil}}(T)$ parameterization from Eq. A1 to simulated dust concentrations. Dust concentrations are simulated using a global configuration of the Met Office Unified Model (Brown et al., 2012b) version 12.1 which includes Global Atmosphere version 8.0 and Global Land model version 9.0 (Willett et al., 2020). The configuration we use is described in detail by Jones et al. (2022) with the addition of dust in a super-coarse aerosol mode. The emission, advection, and

500   removal of aerosol is simulated by the UK Chemistry and Aerosol (UKCA-mode) model (Mann et al., 2010) which includes a prognostic two-moment aerosol microphysics scheme. In this configuration of UKCA-mode, aerosol components (sea-salt, sulphate, black carbon, organic carbon, and dust) are represented by log-normally distributed aerosol modes. Dust is present in the accumulation, coarse, and super-coarse modes. Global dust emission parameters (horiz_d, us_{am}, and sm_{corr}) were tuned to global observations of dust aerosol optical depths, dust size distributions, surface dust concentrations, and dust deposition

505   fluxes (Woodward et al., 2022). The resulting values are $\text{horiz}_d = 6.0$, $\text{us}_{\text{am}} = 1.45$, and $\text{sm}_{\text{corr}} = 0.7$.

A simulation was run from 2018 to 2024, with U and V wind components above the boundary layer nudged to 6-hourly ERA5 reanalysis, and sea surface properties and fluxes represented by observed climatologies of sea surface temperature and sea ice content. The simulated dust aerosol size distributions were extracted for a region ($62.8°\text{W} - 51.6°\text{W}$, $53.1°\text{N} - 60.6°\text{N}$) and time period ($23/10/22 - 5/11/22$) consistent with the M-Phase campaign. The dust INP number concentration ($N_{\text{dust}-\text{INP}}$)

510   is calculated at each temperature T and in each dust size bin i following the singular description (Murray et al., 2012; DeMott et al., 2015; Vali, 2008) using

$$N_{\text{dust}-\text{INP}_i}(T) = N_{\text{dust}_i}(1 - e^{n_{s,\text{soil}}(T)\pi d^2}), \tag{B1}$$

where N_{dust_i} is the dust number concentration in each size bin (L^{-1} of air) and d is the mean diameter of the bin. The bins are summed to obtain the total $N_{\text{dust}-\text{INP}}$ for each grid box and for each time step (3 hr) of the time series. This is repeated

515   for three model levels (surface, 1 km and 2 km) and a mean taken over the three. A polynomial fit to all values of $N_{\text{dust}-\text{INP}}$ is used to produce a parameterization for $N_{\text{INP,M}-\text{Phase}}(T)$ which is described by

$$\log_{10} N_{\text{INP,M}-\text{Phase}}(T) = -4.591 - 0.5284T - 3.341 \times 10^{-2}T^2 - 1.249 \times 10^{-3}T^3 - 1.579 \times 10^{-5}T^4, \tag{B2}$$

where $N_{\text{INP,M}-\text{Phase}}$ has units L^{-1} of air and T is in $°\text{C}$.

## Appendix C: Kernel selection and testing results of GP emulators
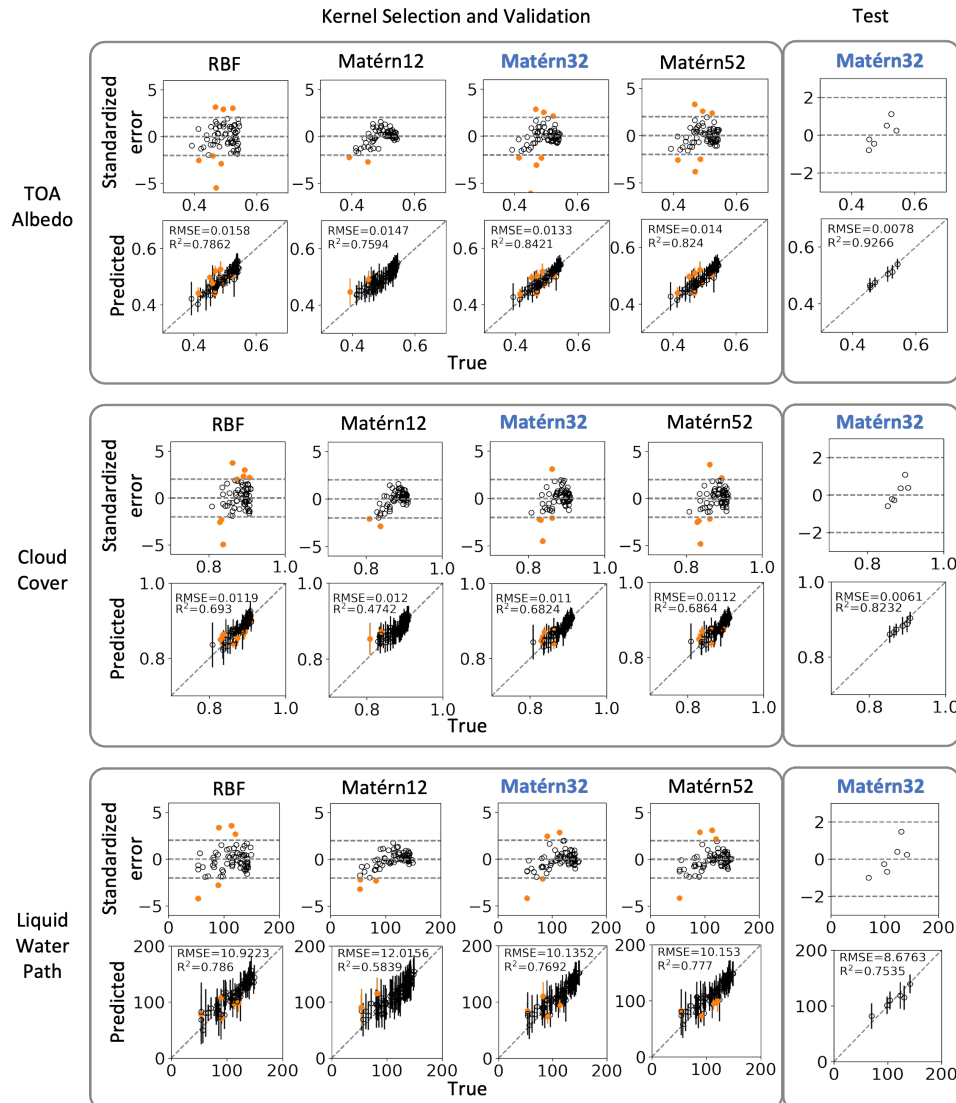
Figure C1. Kernel selection and testing results of the GP emulators on TOA albedo, cloud cover, and LWP in the Sc model analysis region. Points in orange indicate a failed emulated point in the standardized error check. The kernel name highlighted in blue indicates that the kernel was selected and the testing results are from comparing the emulator trained with the selected kernel with the testing dataset.
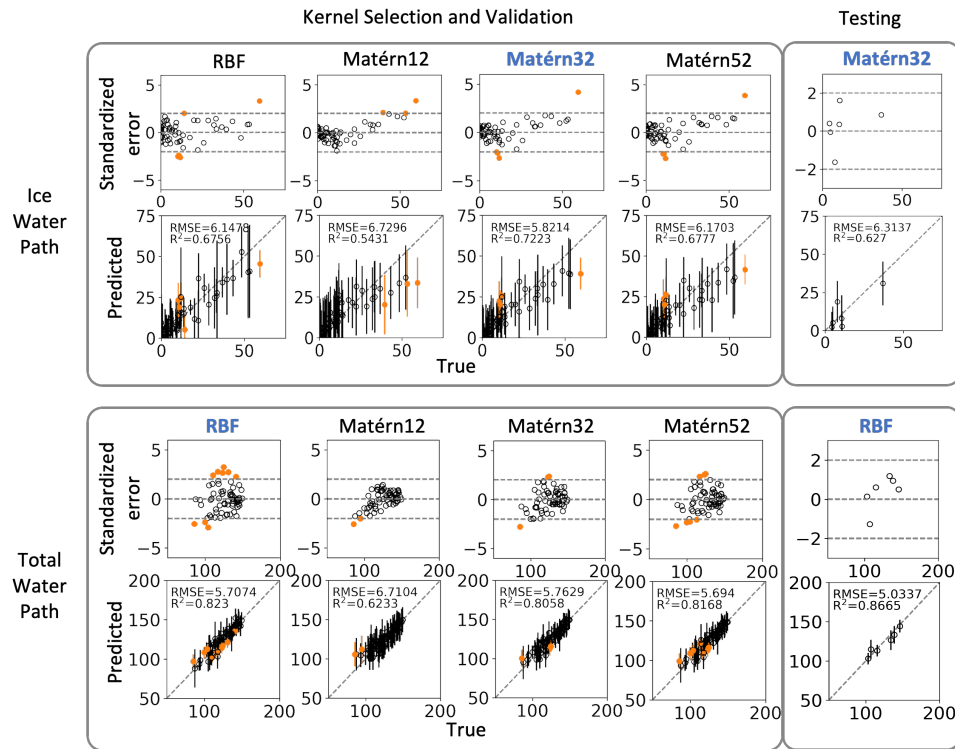
Figure C2. Kernel selection and testing results of the GP emulators on IWP and TWP in the Sc model analysis region. Points in orange indicate a failed emulated point in the standardized error check. The kernel name highlighted in blue indicates that the kernel was selected and the testing results are from comparing the emulator trained with the selected kernel with the testing dataset.
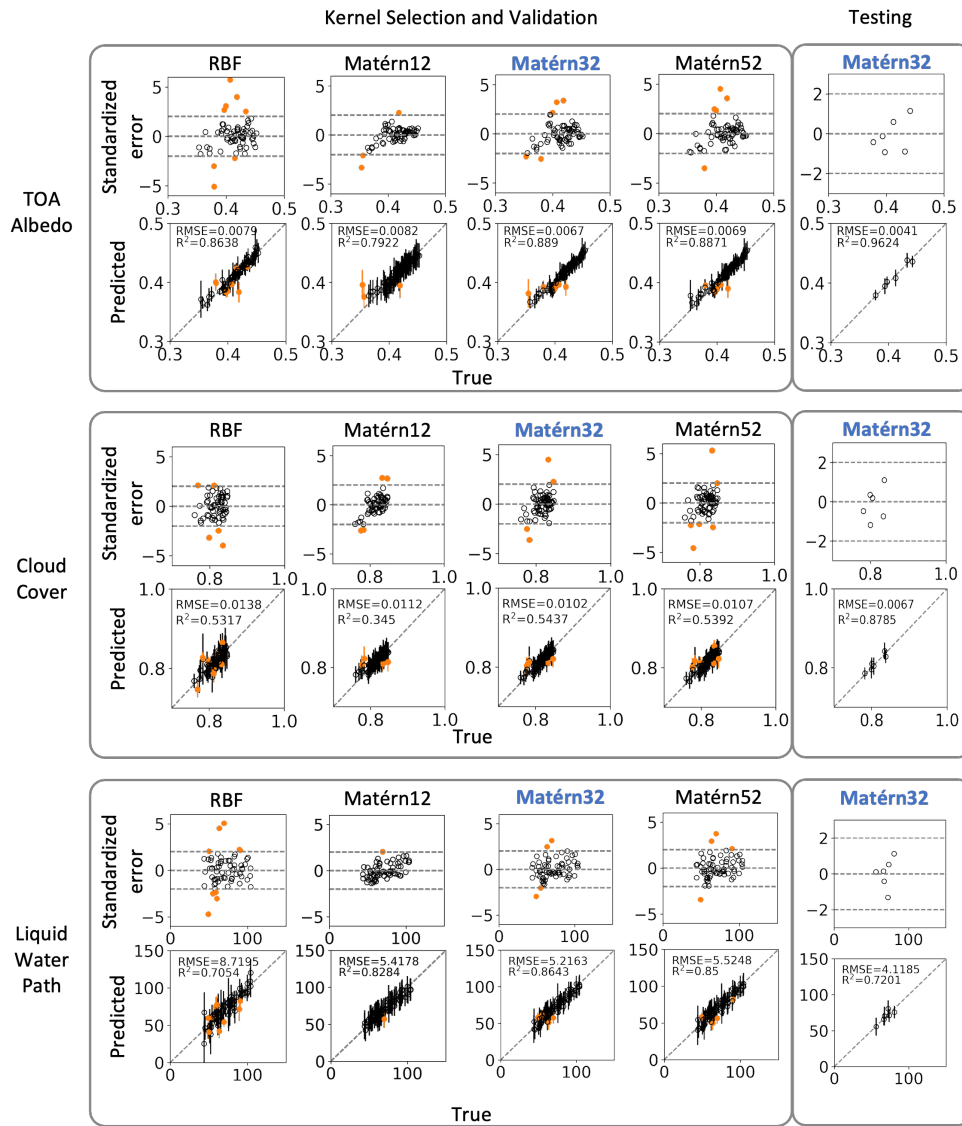
Figure C3. Kernel selection and testing results of the GP emulators on TOA albedo, cloud cover, and LWP in the Cu model analysis region. Points in orange indicate a failed emulated point in the standardized error check. The kernel name highlighted in blue indicates that the kernel was selected and the testing results are from comparing the emulator trained with the selected kernel with the testing dataset.
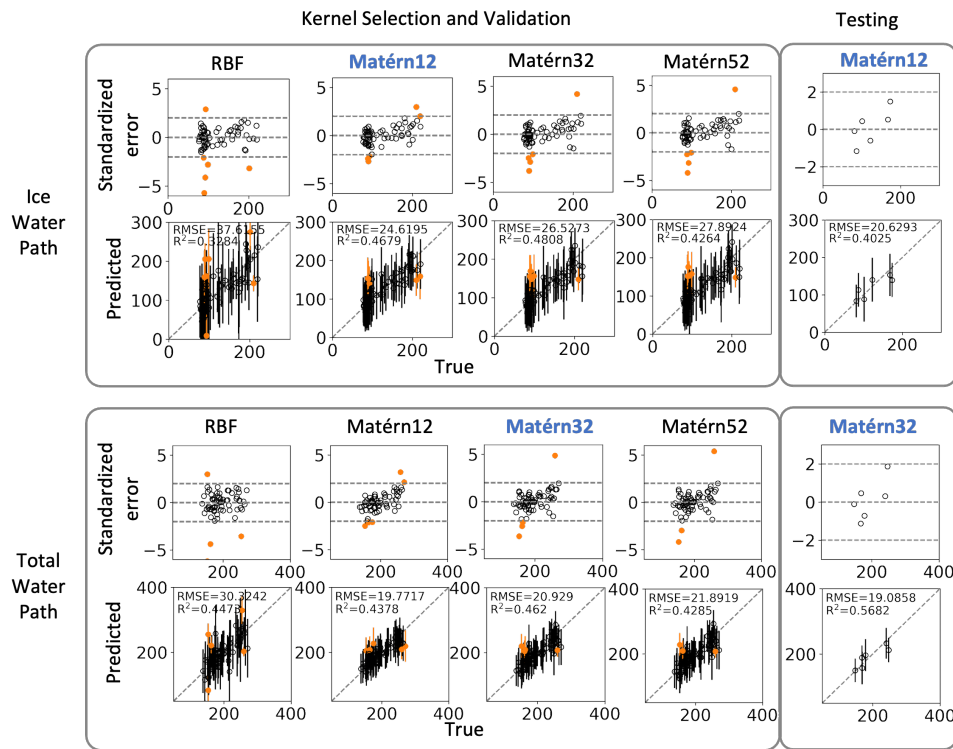
Figure C4. Kernel selection and testing results of the GP emulators on IWP and TWP in the Cu model analysis region. Points in orange indicate a failed emulated point in the standardized error check. The kernel name highlighted in blue indicates that the kernel was selected and the testing results are from comparing the emulator trained with the selected kernel with the testing dataset.

520 **Appendix D: Flow chart for methods involved in this work**
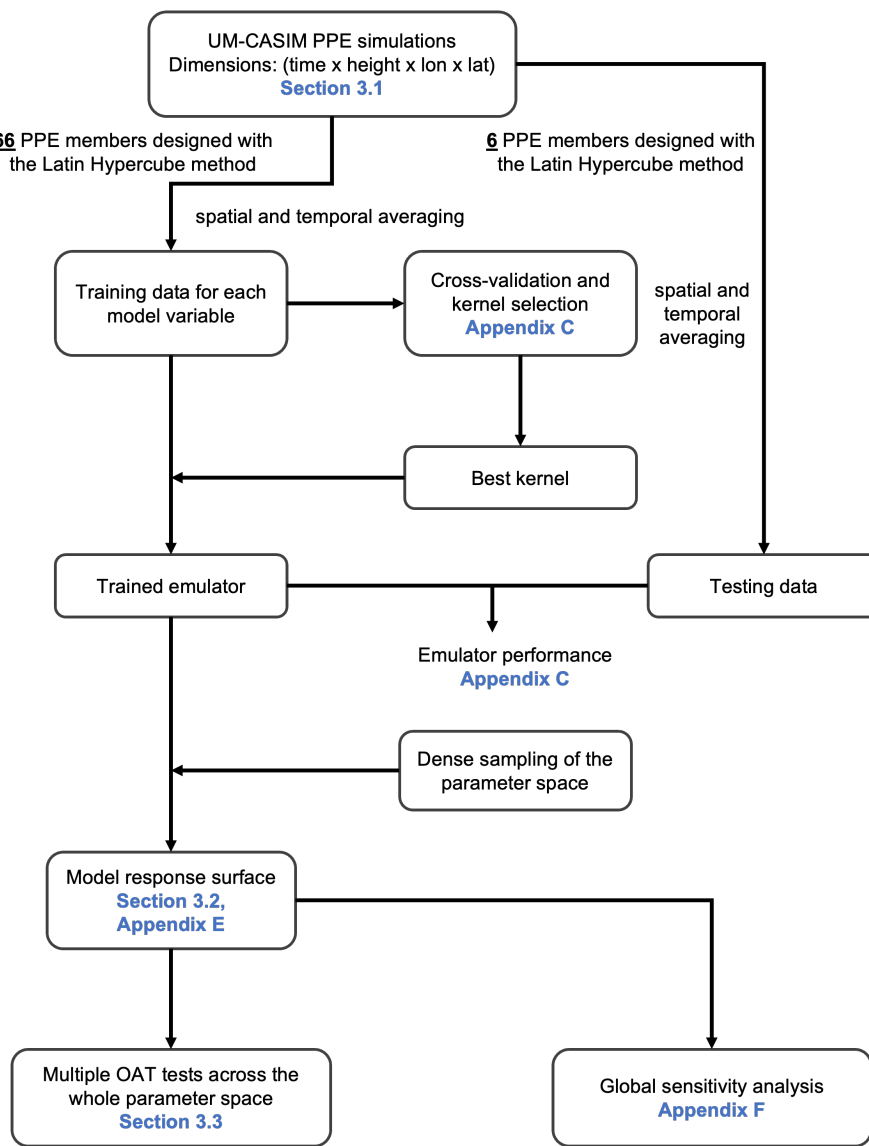
Figure D1. Flowchart for methods involved in this work. The sections include the corresponding results are highlighted in blue.

Appendix E: Simple illustration of linear and non-linear joint effects between two parameters
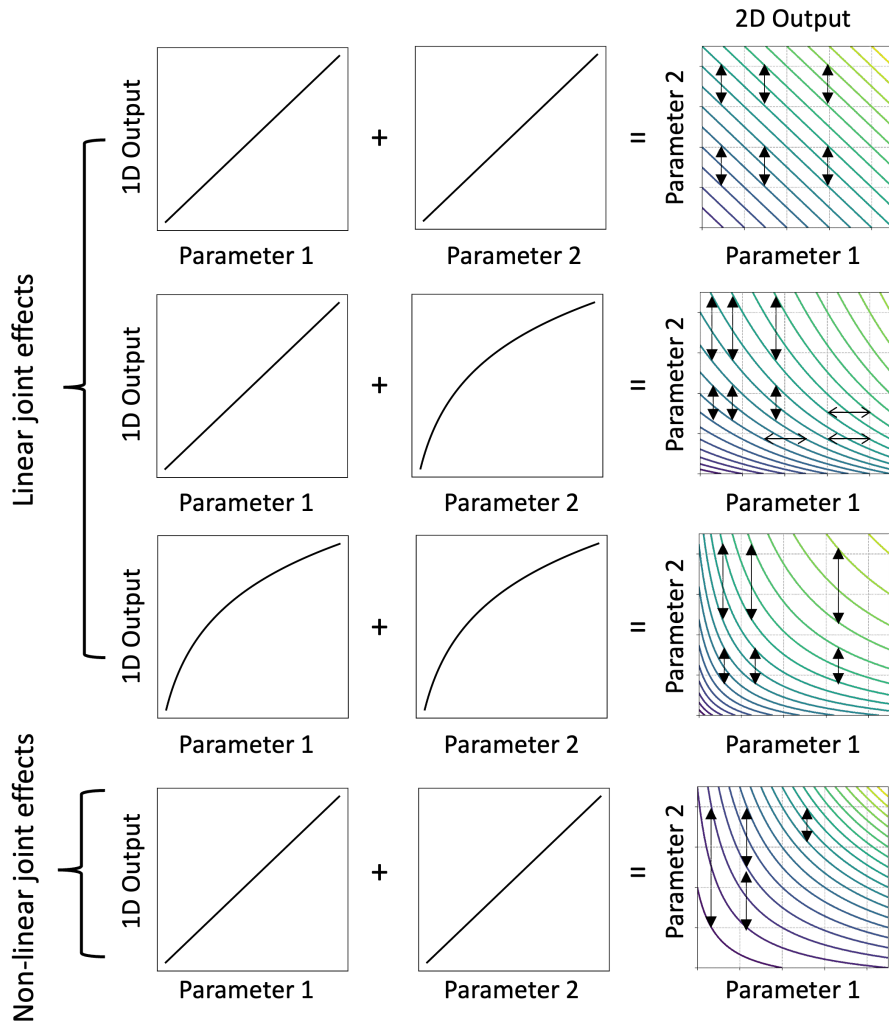
Figure E1. A simple illustration of linear and non-linear joint effects between two parameters. This diagram is adapted from Figure 3.3 in the work of Sansom (2023). With linear joint effects, the effect of changing one parameter on the model output is independent of the value of the other parameter. With non-linear joint effects, the effect of changing one parameter on the model output is then dependent on the value of the other parameter. The length of the arrows shown in the 2D output represents the variation needed for a parameter to across three contour lines. All the contour lines shown here are with linear scale.

Appendix F: Additional paired-projection figures from GP emulators
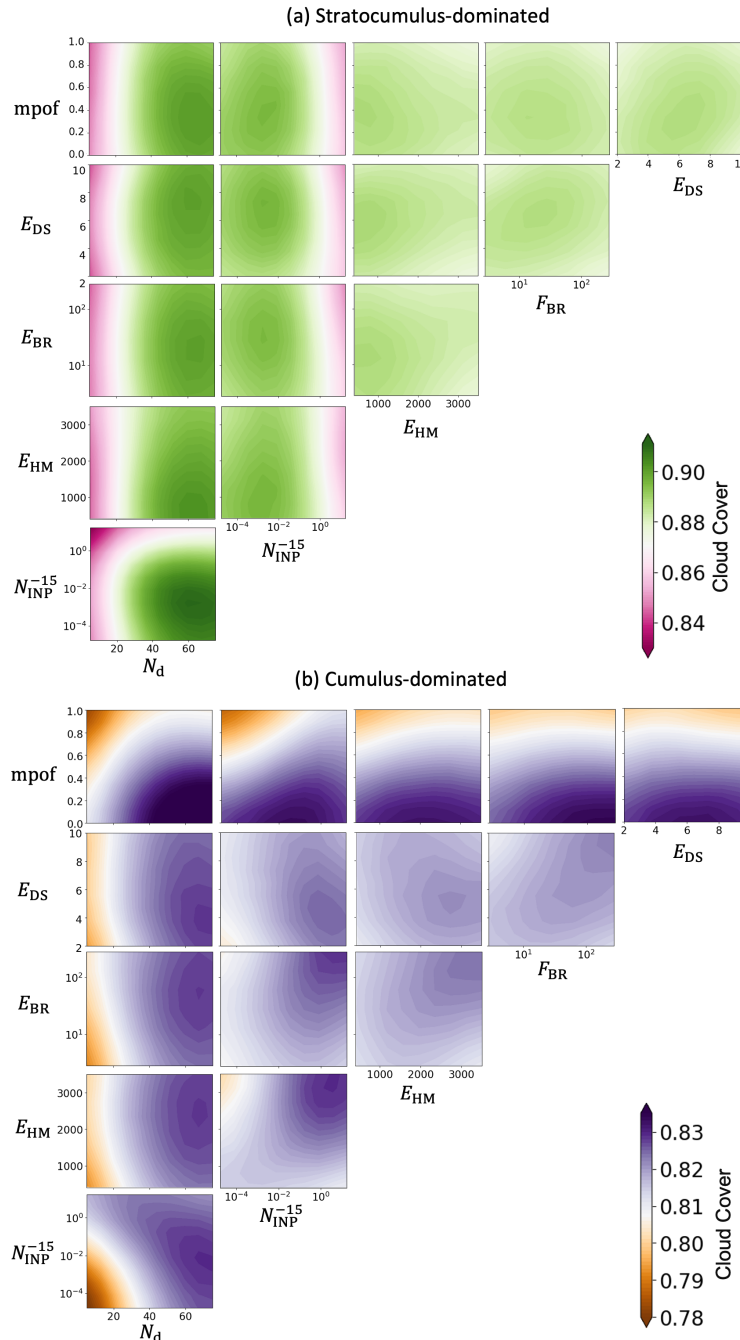
Figure F1. Projected mean model responses of cloud cover to paired parameters in (a) Sc region and (b) Cu region.
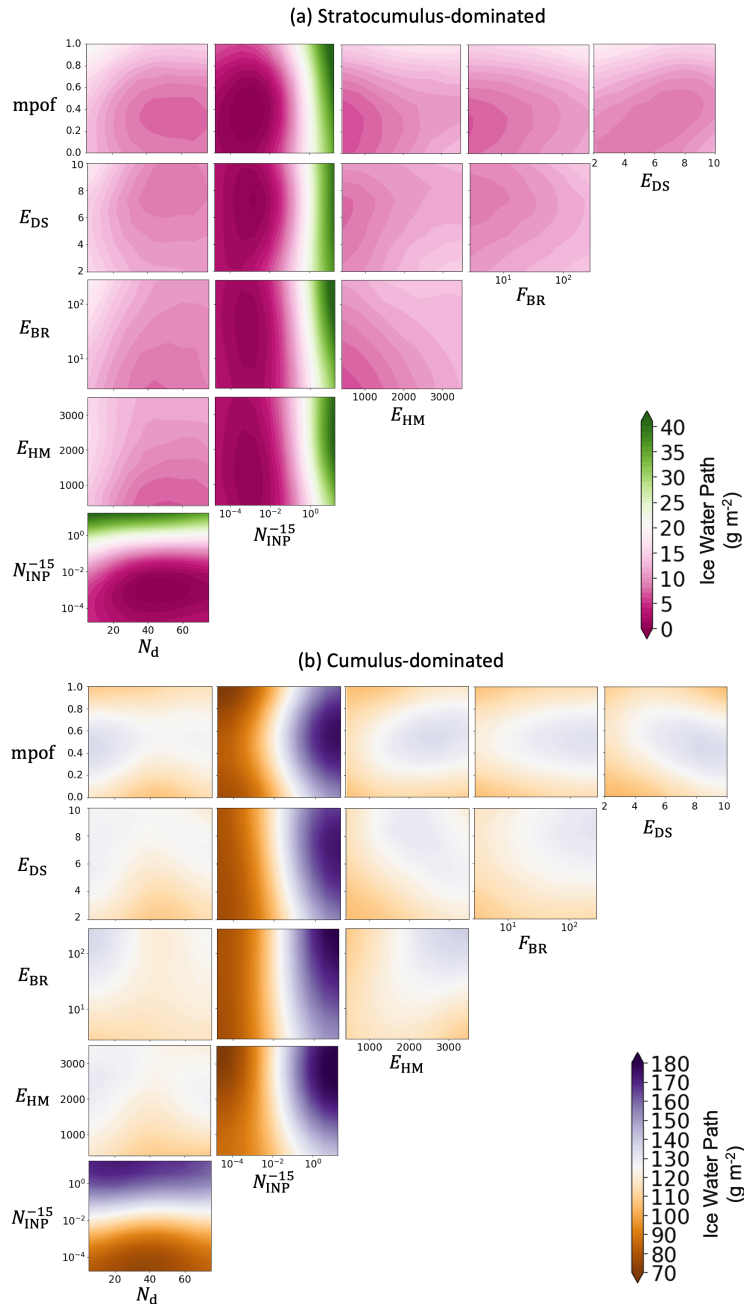
Figure F2. Projected mean model responses of all-sky IWP (ice water path) to paired parameters in (a) Sc region and (b) Cu region.
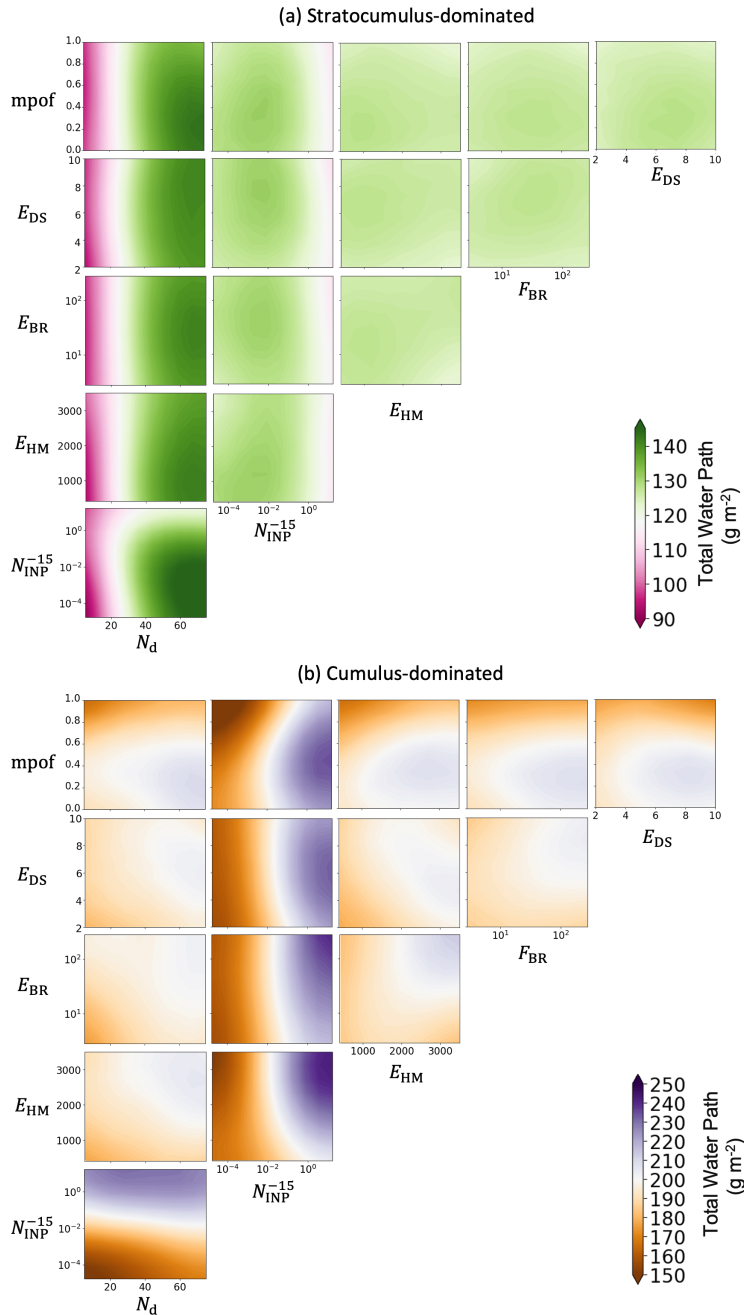
Figure F3. Projected mean model responses of all-sky TWP (total water path) to paired parameters in (a) Sc region and (b) Cu region.

Appendix G: Results from the global sensitivity analysis

A variance-based sensitivity analysis was also performed to quantify the sensitivities of model variables to the perturbed parameters based on a dense sampling of the emulated parameter space (Saltelli et al., 2000). We used the Sobol' method (Saltelli et al., 2000) with the Python library SALib (Usher et al., 2016) to calculate the sensitivity indices. The first-order sensitivity index measures the main effect of each parameter on a model variable. The total sensitivity index includes both the main effect and any additional effects from interactions with other parameters. Therefore, the difference between the total index and the first-order index indicates how much of a parameter's influence comes from its interactions with other parameters (interactive effects) (Johnson et al., 2015).

Figure F1 shows the sensitivity indices over the whole parameter space. This comparison allows us to quantitatively investigate the dominant parameters for the cloud properties of interest over the 6-D parameter space, rather than, as shown in the paired projections, limiting to the values averaged across the parameter space for the non-paired parameters.

N_d dominates the TOA albedo in both regions and exerts strong influences on cloud cover and LWP. In contrast, IWP in both regions has little sensitivity to the perturbations of N_d. The strong control of N_d over the TOA albedo suggests that an accurate representation of N_d and associated processes, including background aerosol fields, droplet activation of CCN and in-cloud processing of CCN, is essential to accurately represent these mixed-phase clouds in simulations.

N_{INP}^{-15} has a strong control of all-sky LWP and IWP in both regions, but its effect on TOA albedo is much weaker compared to N_d. In the Cu region, a high N_{INP}^{-15} leads to a reduction in LWP but also an increase in IWP, therefore, its overall influence on TWP is compensated. Although N_{INP}^{-15} strongly influences LWP in both cases, its weaker influence on TOA albedo compared to the influence from N_d suggests that, in this CAO case, the Twomey effect associated with perturbations in N_d plays a more dominant role in determining the radiative properties of CAO clouds. As a result, TOA albedo exhibits more sensitivity to perturbations of N_d than to N_{INP}^{-15}. It is also worth noting here that because the cloud temperature in our case is warm (with a cloud top temperature around -15 °C), the INP concentrations are generally low. Most of the perturbed N_{INP}^{-15} is below 1 L^{-1}, which is smaller than the threshold suggested from Vergara-Temprado et al. (2018) for INP to have a strong effect on TOA albedo.

In this CAO case, all SIP parameters (E_{HM}, E_{BR} and E_{DS}) have generally weak influence on the cloud radiative properties in both regions, compared to other parameters. Comparing the different regions shows that the influence from SIP processes on cloud properties is relatively enhanced in the Cu region, as the clouds deepen and IWP increases with more snow and graupel formations. Most of their influences on cloud cover are interactive effects, suggesting an additional dependency on other parameters. Among the three SIP parameters, E_{HM} has the strongest influence on LWP, IWP and TWP. This occurs because most cloud temperatures in this case (ranging from -5 to -15 °C) are warmer than the peak temperature for the ice-ice collision (-21 °C) and droplet shattering (-15 °C) processes, but within the temperature range for the HM process (-7.5 °C to -2.5 °C) which peaks at -5 °C. Therefore, the sensitivities of cloud properties to the parameters shown here are case specific; this point will be further discussed in the Discussion section.

The influences of mpof are weak in the Sc region, but become much stronger in the Cu region for cloud cover and LWP, where IWP increased a lot compared to the ones in the Sc region. Its effects on TOA albedo are also enhanced in the Cu region, but much weaker compared to the those from N_d. The explanation is similar to N_{INP}^{-15}, as in this case, the radiative properties of CAO clouds are dominated by the Twomey effect associated with perturbations in N_d, rather than the change in LWP. The mpof parameter controls the extent to which liquid and ice hydrometeors interact with each other, and our results suggest that for cloud cover and LWP in the Cu region, it is important to have a good representation of the degree of overlap between ice and liquid hydrometeors. However, mpof remains poorly constrained in models (Abel et al., 2017; Korolev and Milbrandt, 2022; Evans et al., 2025) and can lead to large uncertainties in estimating mixed-phase cloud behaviours under the warming climate and their influences to the Earth's energy budget.

Figure G1. Sensitivity indices of all the perturbed parameters for TOA albedo (unitless), cloud cover (unitless), all-sky LWP $(\mathrm{g\,m^{-2}})$, all-sky IWP $(\mathrm{g\,m^{-2}})$ and all-sky TWP $(\mathrm{g\,m^{-2}})$. Each sensitivity index consists of the first-order, main effect (solid fill) and the second-order, interactive effects (dashed). Indices are shown separately for the Sc (left column) and Cu (right column) regions.

References

Abel, S. J., Boutle, I. A., Waite, K., Fox, S., Brown, P. R. A., Cotton, R., Lloyd, G., Choularton, T. W., and Bower, K. N.: The Role of Precipitation in Controlling the Transition from Stratocumulus to Cumulus Clouds in a Northern Hemisphere Cold-Air Outbreak, Journal of the Atmospheric Sciences, 74, 2293 – 2314, https://doi.org/10.1175/JAS-D-16-0362.1, 2017.

Albrecht, B. A.: Aerosols, Cloud Microphysics, and Fractional Cloudiness, Science, 245, 1227–1230, https://doi.org/10.1126/science.245.4923.1227, 1989.

Baran, A. J., Manners, J., Field, P. R., Furtado, K., and Hill, A.: A consistent coupling of two-moment microphysics and bulk ice optical properties, and its impact on radiation in a regional weather model, Quarterly Journal of the Royal Meteorological Society, 151, e5025, https://doi.org/https://doi.org/10.1002/qj.5025, 2025.

Barr, S. L., Wyld, B., McQuaid, J. B., Neely III, R. R., and Murray, B. J.: Southern Alaska as a source of atmospheric mineral dust and ice-nucleating particles, Science Advances, 9, eadg3708, https://doi.org/10.1126/sciadv.adg3708, publisher: American Association for the Advancement of Science, 2023.

Bastos, L. S. and O'Hagan, A.: Diagnostics for Gaussian Process Emulators, Technometrics, 51, 425–438, https://doi.org/10.1198/TECH.2009.08019, 2009.

Beven, K.: A manifesto for the equifinality thesis, Journal of Hydrology, 320, 18–36, https://doi.org/https://doi.org/10.1016/j.jhydrol.2005.07.007, 2006.

Bigg, E. K.: The formation of atmospheric ice crystals by the freezing of droplets, Quarterly Journal of the Royal Meteorological Society, 79, 510–519, https://doi.org/https://doi.org/10.1002/qj.49707934207, 1953.

Bodas-Salcedo, A., Mulcahy, J. P., Andrews, T., Williams, K. D., Ringer, M. A., Field, P. R., and Elsaesser, G. S.: Strong Dependence of Atmospheric Feedbacks on Mixed-Phase Microphysics and Aerosol-Cloud Interactions in HadGEM3, Journal of Advances in Modeling Earth Systems, 11, 1735–1758, https://doi.org/doi.org/10.1029/2019MS001688, 2019.

Brown, A., Milton, S., Cullen, M., Golding, B., Mitchell, J., and Shelly, A.: Unified Modeling and Prediction of Weather and Climate: A 25-Year Journey, Bulletin of the American Meteorological Society, 93, 1865–1877, https://doi.org/10.1175/BAMS-D-12-00018.1, 2012a.

Brown, A., Milton, S., Cullen, M., Golding, B., Mitchell, J., and Shelly, A.: Unified Modeling and Prediction of Weather and Climate: A 25-Year Journey, Bulletin of the American Meteorological Society, 93, 1865–1877, https://doi.org/10.1175/BAMS-D-12-00018.1, publisher: American Meteorological Society Section: Bulletin of the American Meteorological Society, 2012b.

Brümmer, B.: Boundary-layer modification in wintertime cold-air outbreaks from the Arctic sea ice, Boundary-Layer Meteorology, 80, 109–125, https://doi.org/10.1007/BF00119014, 1996.

Brümmer, B.: Roll and Cell Convection in Wintertime Arctic Cold-Air Outbreaks, Journal of the Atmospheric Sciences, 56, 2613 – 2636, https://doi.org/10.1175/1520-0469(1999)056<2613:RACCIW>2.0.CO;2, 1999.

Bush, M., Flack, D. L. A., Lewis, H. W., Bohnenstengel, S. I., Short, C. J., Franklin, C., Lock, A. P., Best, M., Field, P., McCabe, A., Van Weverberg, K., Berthou, S., Boutle, I., Brooke, J. K., Cole, S., Cooper, S., Dow, G., Edwards, J., Finnenkoetter, A., Furtado, K., Halladay, K., Hanley, K., Hendry, M. A., Hill, A., Jayakumar, A., Jones, R. W., Lean, H., Lee, J. C. K., Malcolm, A., Mittermaier, M., Mohandas, S., Moore, S., Morcrette, C., North, R., Porson, A., Rennie, S., Roberts, N., Roux, B., Sanchez, C., Su, C.-H., Tucker, S., Vosper, S., Walters, D., Warner, J., Webster, S., Weeks, M., Wilkinson, J., Whitall, M., Williams, K. D., and Zhang, H.: The third Met Office Unified Model–JULES Regional Atmosphere and Land Configuration, RAL3, Geoscientific Model Development, 18, 3819–3855, https://doi.org/10.5194/gmd-18-3819-2025, 2025.

Carslaw, K. S., Regayre, L. A., Proske, U., Gettelman, A., Sexton, D. M. H., Qian, Y., Marshall, L., Wild, O., van Lier-Walqui, M., Oertel, A., Peatier, S., Yang, B., Johnson, J. S., Li, S., McCoy, D. T., Sanderson, B. M., Williamson, C. J., Elsaesser, G. S., Yamazaki, K., and Booth, B. B. B.: Opinion: The importance and future development of perturbed parameter ensembles in climate and atmospheric science,

620   EGUsphere, 2025, 1–31, https://doi.org/10.5194/egusphere-2025-4341, 2025.

Ceppi, P., Brient, F., Zelinka, M. D., and Hartmann, D. L.: Cloud feedback mechanisms and their representation in global climate models, WIREs Climate Change, 8, e465, https://doi.org/10.1002/wcc.465, 2017.

Clarke, S. J., Abel, S. J., Nott, G. J., Raif, E. N., Tarn, M. D., Biggart, M., Wu, H., Ashmore, D. W., Barr, S. L., Barrett, P. A., Bower, K. N., Bowles, J., Connolly, P. J., Cotton, R., Evans, M. D., Flynn, M., Foster, P. B., Fox, S., Gallagher, M. W., Hu, K., Kent, J., Lloyd, G.,

625   Marsden, N. A., McQuaid, J. B., Robinson, J., Tiddeman, D., Wilson, A., Wivell, K., Field, P. R., Choularton, T. W., and Murray, B. J.: Marine cold-air outbreaks over the Norwegian-Barents and Labrador seas: observational datasets from the ACAO and M-Phase aircraft campaigns, manuscript submitted for publication, 2025.

Creamean, J. M., Kirpes, R. M., Pratt, K. A., Spada, N. J., Maahn, M., de Boer, G., Schnell, R. C., and China, S.: Marine and terrestrial influences on ice nucleating particles during continuous springtime measurements in an Arctic oilfield location, Atmospheric Chemistry

630   and Physics, 18, 18 023–18 042, https://doi.org/10.5194/acp-18-18023-2018, 2018.

Creamean, J. M., Cross, J. N., Pickart, R., McRaven, L., Lin, P., Pacini, A., Hanlon, R., Schmale, D. G., Ceniceros, J., Aydell, T., Colombi, N., Bolger, E., and DeMott, P. J.: Ice Nucleating Particles Carried From Below a Phytoplankton Bloom to the Arctic Atmosphere, Geophysical Research Letters, 46, 8572–8581, https://doi.org/10.1029/2019GL083039, 2019.

de Roode, S. R., Frederikse, T., Siebesma, A. P., Ackerman, A. S., Chylik, J., Field, P. R., Fricke, J., Gryschka, M., Hill, A., Hon-

635   nert, R., Krueger, S. K., Lac, C., Lesage, A. T., and Tomassini, L.: Turbulent Transport in the Gray Zone: A Large Eddy Model Intercomparison Study of the CONSTRAIN Cold Air Outbreak Case, Journal of Advances in Modeling Earth Systems, 11, 597–623, https://doi.org/10.1029/2018MS001443, 2019.

DeMott, P. J., Prenni, A. J., McMeeking, G. R., Sullivan, R. C., Petters, M. D., Tobo, Y., Niemand, M., Möhler, O., Snider, J. R., Wang, Z., and Kreidenweis, S. M.: Integrating laboratory and field data to quantify the immersion freezing ice nucleation activity of mineral

640   dust particles, Atmospheric Chemistry and Physics, 15, 393–409, https://doi.org/10.5194/acp-15-393-2015, publisher: Copernicus GmbH, 2015.

DeMott, P. J., Hill, T. C. J., McCluskey, C. S., Prather, K. A., Collins, D. B., Sullivan, R. C., Ruppel, M. J., Mason, R. H., Irish, V. E., Lee, T., Hwang, C. Y., Rhee, T. S., Snider, J. R., McMeeking, G. R., Dhaniyala, S., Lewis, E. R., Wentzell, J. J. B., Abbatt, J., Lee, C., Sultana, C. M., Ault, A. P., Axson, J. L., Martinez, M. D., Venero, I., Santos-Figueroa, G., Stokes, M. D., Deane, G. B., Mayol-Bracero, O. L.,

645   Grassian, V. H., Bertram, T. H., Bertram, A. K., Moffett, B. F., and Franc, G. D.: Sea spray aerosol as a unique source of ice nucleating particles, Proceedings of the National Academy of Sciences, 113, 5797–5803, https://doi.org/10.1073/pnas.1514034112, 2016.

Evans, M. D., Abel, S. J., Field, P. R., Finney, D. L., Lloyd, G., Cotton, R. J., Smith, D. K., Murray, B. J., and Huang, X.: Characterising the spatial overlap between liquid and ice in mixed-phase clouds, Quarterly Journal of the Royal Meteorological Society, n/a, e5041, https://doi.org/https://doi.org/10.1002/qj.5041, 2025.

650 Field, P. R., Cotton, R. J., McBeath, K., Lock, A. P., Webster, S., and Allan, R. P.: Improving a convection-permitting model simulation of a cold air outbreak, Quarterly Journal of the Royal Meteorological Society, 140, 124–138, https://doi.org/10.1002/qj.2116, 2014.

Field, P. R., Brožková, R., Chen, M., Dudhia, J., Lac, C., Hara, T., Honnert, R., Olson, J., Siebesma, P., de Roode, S., Tomassini, L., Hill, A., and McTaggart-Cowan, R.: Exploring the convective grey zone with regional simulations of a cold air outbreak, Quarterly Journal of the Royal Meteorological Society, 143, 2537–2555, https://doi.org/https://doi.org/10.1002/qj.3105, 2017.

655   Field, P. R., Hill, A., Shipway, B., Furtado, K., Wilkinson, J., Miltenberger, A., Gordon, H., Grosvenor, D. P., Stevens, R., and Van Weverberg,
         K.: Implementation of a Double Moment Cloud Microphysics Scheme in the UK Met Office Regional Numerical Weather Prediction
         Model, Quarterly Journal of the Royal Meteorological Society, https://doi.org/10.1002/qj.4414, 2023.

      Fletcher, J., Mason, S., and Jakob, C.: The Climatology, Meteorology, and Boundary Layer Structure of Marine Cold Air Outbreaks in Both
         Hemispheres, Journal of Climate, 29, 1999–2014, https://doi.org/10.1175/JCLI-D-15-0268.1, 2016a.

660   Fletcher, J. K., Mason, S., and Jakob, C.: A Climatology of Clouds in Marine Cold Air Outbreaks in Both Hemispheres, Journal of Climate,
         29, 6677 – 6692, https://doi.org/10.1175/JCLI-D-15-0783.1, 2016b.

      Forster, P., Storelvmo, T., Armour, K., Collins, W., Dufresne, J. L., Frame, D., Lunt, D. J., Mauritsen, T., Palmer, M. D., Watanabe, M., Wild,
         M., and Zhang, H.: The Earth's Energy Budget, Climate Feedbacks, and Climate Sensitivity, in: Climate Change 2021: The Physical
         Science Basis. Contribution of Working Group I to the Sixth Assessment Report of the Intergovernmental Panel on Climate Change,
665   edited by Masson-Delmotte, V., Zhai, P., Pirani, A., Connors, S. L., Péan, C., Berger, S., Caud, N., Chen, Y., Goldfarb, L., Gomis, M. I.,
         Huang, M., Leitzell, K., Lonnoy, E., Matthews, J. B. R., Maycock, T. K., Waterfield, T., Yelekçi, O., Yu, R., and Zhou, B., book section 7,
         Cambridge University Press, Cambridge, United Kingdom and New York, NY, USA, 2021.

      Franz Conen, Emiliano Stopelli, L. Z.: Clues that decaying leaves enrich Arctic air with ice nucleating particles, Atmospheric Environment,
         Atmospheric Environment, 129, 91–94, https://doi.org/10.1016/j.atmosenv.2016.01.027, 2016.

670   Glassmeier, F., Hoffmann, F., Johnson, J. S., Yamaguchi, T., Carslaw, K. S., and Feingold, G.: An emulator approach to stratocumulus
         susceptibility, Atmospheric Chemistry and Physics, 19, 10 191–10 203, https://doi.org/10.5194/acp-19-10191-2019, 2019.

      Grosvenor, D. P., Sourdeval, O., Zuidema, P., Ackerman, A., Alexandrov, M. D., Bennartz, R., Boers, R., Cairns, B., Chiu, J. C., Christensen,
         M., Deneke, H., Diamond, M., Feingold, G., Fridlind, A., Hünerbein, A., Knist, C., Kollias, P., Marshak, A., McCoy, D., Merk, D.,
         Painemal, D., Rausch, J., Rosenfeld, D., Russchenberg, H., Seifert, P., Sinclair, K., Stier, P., van Diedenhoven, B., Wendisch, M., Werner,
675   F., Wood, R., Zhang, Z., and Quaas, J.: Remote Sensing of Droplet Number Concentration in Warm Clouds: A Review of the Current
         State of Knowledge and Perspectives, Reviews of Geophysics, 56, 409–453, https://doi.org/10.1029/2017RG000593, 2018.

      Hallett, J. and Mossop, S. C.: Production of secondary ice particles during the riming process, Nature, 249, 26–28, 1974.

      Harrison, A. D., Lever, K., Sanchez-Marroquin, A., Holden, M. A., Whale, T. F., Tarn, M. D., McQuaid, J. B., and Murray, B. J.: The
         ice-nucleating ability of quartz immersed in water and its atmospheric importance compared to K-feldspar, Atmospheric Chemistry and
680   Physics, 19, 11 343–11 361, https://doi.org/10.5194/acp-19-11343-2019, publisher: Copernicus GmbH, 2019.

      Hartmann, M., Adachi, K., Eppers, O., Haas, C., Herber, A., Holzinger, R., Hünerbein, A., Jäkel, E., Jentzsch, C., van Pinxteren, M., Wex, H.,
         Willmes, S., and Stratmann, F.: Wintertime Airborne Measurements of Ice Nucleating Particles in the High Arctic: A Hint to a Marine, Bio-
         genic Source for Ice Nucleating Particles, Geophysical Research Letters, 47, e2020GL087 770, https://doi.org/10.1029/2020GL087770,
         2020.

685   Hartmann, M., Gong, X., Kecorius, S., van Pinxteren, M., Vogl, T., Welti, A., Wex, H., Zeppenfeld, S., Herrmann, H., Wiedensohler, A., and
         Stratmann, F.: Terrestrial or marine – indications towards the origin of ice-nucleating particles during melt season in the European Arctic
         up to 83.7° N, Atmospheric Chemistry and Physics, 21, 11 613–11 636, https://doi.org/10.5194/acp-21-11613-2021, 2021.

      Hawker, R. E., Miltenberger, A. K., Johnson, J. S., Wilkinson, J. M., Hill, A. A., Shipway, B. J., Field, P. R., Murray, B. J., and Carslaw,
         K. S.: Model emulation to understand the joint effects of ice-nucleating particles and secondary ice production on deep convective anvil
690   cirrus, Atmospheric Chemistry and Physics, 21, 17 315–17 343, https://doi.org/10.5194/acp-21-17315-2021, 2021.

Herbert, R. J., Sanchez-Marroquin, A., Grosvenor, D. P., Pringle, K. J., Arnold, S. R., Murray, B. J., and Carslaw, K. S.: Gaps in our understanding of ice-nucleating particle sources exposed by global simulation of the UK Earth System Model, Atmospheric Chemistry and Physics, 25, 291–325, https://doi.org/10.5194/acp-25-291-2025, publisher: Copernicus GmbH, 2025.

Huang, X., Field, P. R., Murray, B. J., Grosvenor, D. P., van den Heuvel, F., and Carslaw, K. S.: Different responses of cold-air outbreak clouds to aerosol and ice production depending on cloud temperature, EGUsphere, 2025, 1–54, https://doi.org/10.5194/egusphere-2024-4070, 2025.

Igel, A. L., van den Heever, S. C., and Johnson, J. S.: Meteorological and Land Surface Properties Impacting Sea Breeze Extent and Aerosol Distribution in a Dry Environment, Journal of Geophysical Research: Atmospheres, 123, 22–37, https://doi.org/10.1002/2017JD027339, 2018.

Irish, V. E., Hanna, S. J., Willis, M. D., China, S., Thomas, J. L., Wentzell, J. J. B., Cirisan, A., Si, M., Leaitch, W. R., Murphy, J. G., Abbatt, J. P. D., Laskin, A., Girard, E., and Bertram, A. K.: Ice nucleating particles in the marine boundary layer in the Canadian Arctic during summer 2014, Atmospheric Chemistry and Physics, 19, 1027–1039, https://doi.org/10.5194/acp-19-1027-2019, 2019.

Johnson, J. S., Cui, Z., Lee, L. A., Gosling, J. P., Blyth, A. M., and Carslaw, K. S.: Evaluating uncertainty in convective cloud microphysics using statistical emulation, Journal of Advances in Modeling Earth Systems, 7, 162–187, https://doi.org/10.1002/2014MS000383, 2015.

Johnson, J. S., Regayre, L. A., Yoshioka, M., Pringle, K. J., Lee, L. A., Sexton, D. M. H., Rostron, J. W., Booth, B. B. B., and Carslaw, K. S.: The importance of comprehensive parameter sampling and multiple observations for robust constraint of aerosol radiative forcing, Atmospheric Chemistry and Physics, 18, 13 031–13 053, https://doi.org/10.5194/acp-18-13031-2018, 2018.

Johnson, J. S., Regayre, L. A., Yoshioka, M., Pringle, K. J., Turnock, S. T., Browse, J., Sexton, D. M. H., Rostron, J. W., Schutgens, N. A. J., Partridge, D. G., Liu, D., Allan, J. D., Coe, H., Ding, A., Cohen, D. D., Atanacio, A., Vakkari, V., Asmi, E., and Carslaw, K. S.: Robust observational constraint of uncertain aerosol processes and emissions in a climate model and the effect on aerosol radiative forcing, Atmospheric Chemistry and Physics, 20, 9491–9524, https://doi.org/10.5194/acp-20-9491-2020, 2020.

Jones, A. C., Hill, A., Hemmings, J., Lemaitre, P., Quérel, A., Ryder, C. L., and Woodward, S.: Below-cloud scavenging of aerosol by rain: a review of numerical modelling approaches and sensitivity simulations with mineral dust in the Met Office's Unified Model, Atmospheric Chemistry and Physics, 22, 11 381–11 407, https://doi.org/10.5194/acp-22-11381-2022, publisher: Copernicus GmbH, 2022.

Karalis, M., Sotiropoulou, G., Abel, S. J., Bossioli, E., Georgakaki, P., Methymaki, G., Nenes, A., and Tombrou, M.: Effects of secondary ice processes on a stratocumulus to cumulus transition during a cold-air outbreak, Atmospheric Research, 277, 106 302, https://doi.org/10.1016/j.atmosres.2022.106302, 2022.

King, L.: Using a small expansion chamber to characterise ice nucleation by high-latitude mineral dusts and volcanic ash, phd, University of Leeds, https://etheses.whiterose.ac.uk/id/eprint/35595/, 2024.

Kolstad, E. W. and Bracegirdle, T. J.: Marine cold-air outbreaks in the future: an assessment of IPCC AR4 model results for the Northern Hemisphere, Climate Dynamics, 30, 871–885, https://doi.org/10.1007/s00382-007-0331-0, 2008.

Kolstad, E. W., Bracegirdle, T. J., and Seierstad, I. A.: Marine cold-air outbreaks in the North Atlantic: temporal distribution and associations with large-scale atmospheric circulation, Climate Dynamics, 33, 187–197, https://doi.org/10.1007/s00382-008-0431-5, 2009.

Korolev, A. and Milbrandt, J.: How Are Mixed-Phase Clouds Mixed?, Geophysical Research Letters, 49, e2022GL099 578, https://doi.org/https://doi.org/10.1029/2022GL099578, 2022.

Korolev, A., McFarquhar, G., Field, P. R., Franklin, C., Lawson, P., Wang, Z., Williams, E., Abel, S. J., Axisa, D., Borrmann, S., Crosier, J., Fugal, J., Krämer, M., Lohmann, U., Schlenczek, O., Schnaiter, M., and Wendisch, M.: Mixed-Phase Clouds: Progress and Challenges, Meteorological Monographs, 58, 5.1 – 5.50, https://doi.org/10.1175/AMSMONOGRAPHS-D-17-0001.1, 2017.

Lee, L. A., Carslaw, K. S., Pringle, K. J., Mann, G. W., and Spracklen, D. V.: Emulation of a complex global aerosol model to quantify sensitivity to uncertain parameters, Atmospheric Chemistry and Physics, 11, 12 253–12 273, https://doi.org/10.5194/acp-11-12253-2011, 2011.

Lee, L. A., Carslaw, K. S., Pringle, K. J., and Mann, G. W.: Mapping the uncertainty in global CCN using emulation, Atmospheric Chemistry and Physics, 12, 9739–9751, https://doi.org/10.5194/acp-12-9739-2012, 2012.

Lee, L. A., Pringle, K. J., Reddington, C. L., Mann, G. W., Stier, P., Spracklen, D. V., Pierce, J. R., and Carslaw, K. S.: The magnitude and causes of uncertainty in global model simulations of cloud condensation nuclei, Atmospheric Chemistry and Physics, 13, 8879–8914, https://doi.org/10.5194/acp-13-8879-2013, 2013.

Lee, L. A., Reddington, C. L., and Carslaw, K. S.: On the relationship between aerosol model uncertainty and radiative forcing uncertainty, Proceedings of the National Academy of Sciences, 113, 5820–5827, https://doi.org/10.1073/pnas.1507050113, 2016.

Leisner, T., Pander, T., Handmann, P., and Kiselev, A.: Secondary ice processes upon heterogeneous freezing of cloud droplets, in: Proceedings of the 14th Conference on Cloud Physics & 14th Conference on Atmospheric Radiation, American Meteorological Society, Boston, MA, USA, https://ams.confex.com/ams/14CLOUD14ATRAD/webprogram/Paper250221.html, presented Monday, 7 July 2014, 11:00 AM, Essex Center/South (Westin Copley Place), 2014.

Li, X.-Y., Wang, H., Chen, J., Endo, S., Kirschler, S., Voigt, C., Crosbie, E., Ziemba, L. D., Painemal, D., Cairns, B., Hair, J. W., Corral, A. F., Robinson, C., Dadashazar, H., Sorooshian, A., Chen, G., Ferrare, R. A., Kleb, M. M., Liu, H., Moore, R., Scarino, A. J., Shook, M. A., Shingler, T. J., Thornhill, K. L., Tornow, F., Xiao, H., and Zeng, X.: Large-Eddy Simulations of Marine Boundary Layer Clouds Associated with Cold-Air Outbreaks during the ACTIVATE Campaign. Part II: Aerosol–Meteorology–Cloud Interaction, Journal of the Atmospheric Sciences, 80, 1025 – 1045, https://doi.org/10.1175/JAS-D-21-0324.1, 2023.

Lock, A. P., Brown, A. R., Bush, M. R., Martin, G. M., and Smith, R. N. B.: A New Boundary Layer Mixing Scheme. Part I: Scheme Description and Single-Column Model Tests, Monthly Weather Review, 128, 3187 – 3199, https://doi.org/10.1175/1520-0493(2000)128<3187:ANBLMS>2.0.CO;2, 2000.

Loeppky, J. L., Sacks, J., and Welch, W. J.: Choosing the Sample Size of a Computer Experiment: A Practical Guide, Technometrics, 51, 366–376, https://doi.org/10.1198/TECH.2009.08040, 2009.

Mann, G. W., Carslaw, K. S., Spracklen, D. V., Ridley, D. A., Manktelow, P. T., Chipperfield, M. P., Pickering, S. J., and Johnson, C. E.: Description and evaluation of GLOMAP-mode: a modal global aerosol microphysics model for the UKCA composition-climate model, Geoscientific Model Development, 3, 519–551, https://doi.org/10.5194/gmd-3-519-2010, publisher: Copernicus GmbH, 2010.

Manners, J., Edwards, J. M., Hill, P., and Thelen, J.-C.: SOCRATES Technical Guide Suite Of Community RAdiative Transfer codes based on Edwards and Slingo, Met Office, FitzRoy Rd, Exeter EX1 3PB, 2023.

Marshall, L., Johnson, J. S., Mann, G. W., Lee, L., Dhomse, S. S., Regayre, L., Yoshioka, M., Carslaw, K. S., and Schmidt, A.: Exploring How Eruption Source Parameters Affect Volcanic Radiative Forcing Using Statistical Emulation, Journal of Geophysical Research: Atmospheres, 124, 964–985, https://doi.org/10.1029/2018JD028675, 2019.

Mason, R. H., Si, M., Chou, C., Irish, V. E., Dickie, R., Elizondo, P., Wong, R., Brintnell, M., Elsasser, M., Lassar, W. M., Pierce, K. M., Leaitch, W. R., MacDonald, A. M., Platt, A., Toom-Sauntry, D., Sarda-Estève, R., Schiller, C. L., Suski, K. J., Hill, T. C. J., Abbatt, J. P. D., Huffman, J. A., DeMott, P. J., and Bertram, A. K.: Size-resolved measurements of ice-nucleating particles at six locations in North America and one in Europe, Atmospheric Chemistry and Physics, 16, 1637–1651, https://doi.org/10.5194/acp-16-1637-2016, 2016.

765   McCluskey, C. S., Niu, Q., Hannay, C., Nusbaumer, J. M., Medeiros, B., McFarquhar, G. M., Chapman, W., Fowler, M. D., Stephens, B., Wang, D., Protat, A., and Mace, G. G.: Mixed Phase Aerosol-Cloud Interactions over the Southern Ocean, in: AGU Fall Meeting Abstracts, vol. 2024 of *AGU Fall Meeting Abstracts*, pp. A54C–01, 2024.

McCoy, I. L., Wood, R., and Fletcher, J. K.: Identifying Meteorological Controls on Open and Closed Mesoscale Cellular Convection Associated with Marine Cold Air Outbreaks, Journal of Geophysical Research: Atmospheres, 122, 11,678–11,702,
770   https://doi.org/doi.org/10.1002/2017JD027031, 2017.

Mitchell, J. F. B., Senior, C. A., and Ingram, W. J.: C02 and climate: a missing feedback?, Nature, 341, 132–134, https://doi.org/10.1038/341132a0, 1989.

MODIS Characterization Support Team (MCST): MODIS 1km Calibrated Radiances Product, MODIS Adaptive Processing System, Goddard Space Flight Center, USA, https://doi.org/10.5067/MODIS/MYD021KM.061, 2017.

775   Morrison, H., van Lier-Walqui, M., Fridlind, A. M., Grabowski, W. W., Harrington, J. Y., Hoose, C., Korolev, A., Kumjian, M. R., Milbrandt, J. A., Pawlowska, H., Posselt, D. J., Prat, O. P., Reimel, K. J., Shima, S.-I., van Diedenhoven, B., and Xue, L.: Confronting the Challenge of Modeling Cloud and Precipitation Microphysics, Journal of Advances in Modeling Earth Systems, 12, e2019MS001 689, https://doi.org/10.1029/2019MS001689, 2020.

Murray, B. J. and the M-Phase Team: Ice production in northern hemisphere cold air-outbreak clouds: two contrasting aircraft campaigns,
780   EGU General Assembly 2024, Vienna, Austria, 14–19 Apr 2024, EGU24-11598, https://doi.org/10.5194/egusphere-egu24-11598, 2024.

Murray, B. J., O'Sullivan, D., Atkinson, J. D., and Webb, M. E.: Ice nucleation by particles immersed in supercooled cloud droplets, Chemical Society Reviews, 41, 6519–6554, https://doi.org/10.1039/C2CS35200A, publisher: The Royal Society of Chemistry, 2012.

Murray, B. J., Carslaw, K. S., and Field, P. R.: Opinion: Cloud-phase climate feedback and the importance of ice-nucleating particles, Atmospheric Chemistry and Physics, 21, 665–679, https://doi.org/10.5194/acp-21-665-2021, 2021.

785   Niu, Q., McCluskey, C., and McFarquhar, G. M.: Marine Boundary Layer Cloud Condensation Nuclei Bias Over the Southern Ocean: Comparisons Between the Community Atmosphere Model 6 and Field Observations, Journal of Geophysical Research: Atmospheres, 130, e2024JD042 734, https://doi.org/https://doi.org/10.1029/2024JD042734, 2025.

Oakley, J. and O'Hagan, A.: Bayesian inference for the uncertainty distribution of computer model outputs, Biometrika, 89, 769–784, https://doi.org/10.1093/biomet/89.4.769, 2002.

790   O'Sullivan, D., Murray, B. J., Malkin, T. L., Whale, T. F., Umo, N. S., Atkinson, J. D., Price, H. C., Baustian, K. J., Browse, J., and Webb, M. E.: Ice nucleation by fertile soil dusts: relative importance of mineral and biogenic components, Atmospheric Chemistry and Physics, 14, 1853–1867, https://doi.org/10.5194/acp-14-1853-2014, publisher: Copernicus GmbH, 2014.

O'Hagan, A.: Bayesian analysis of computer code outputs: A tutorial, Reliability Engineering System Safety, 91, 1290–1300, https://doi.org/10.1016/j.ress.2005.11.025, 2006.

795   Paramonov, M., David, R. O., Kretzschmar, R., and Kanji, Z. A.: A laboratory investigation of the ice nucleation efficiency of three types of mineral and soil dust, Atmospheric Chemistry and Physics, 18, 16 515–16 536, https://doi.org/10.5194/acp-18-16515-2018, publisher: Copernicus GmbH, 2018.

Park, J. M., van den Heever, S. C., Igel, A. L., Grant, L. D., Johnson, J. S., Saleeby, S. M., Miller, S. D., and Reid, J. S.: Environmental Controls on Tropical Sea Breeze Convection and Resulting Aerosol Redistribution, Journal of Geophysical Research: Atmospheres, 125,
800   e2019JD031 699, https://doi.org/10.1029/2019JD031699, 2020.

Phillips, V. T. J., Yano, J.-I., and Khain, A.: Ice Multiplication by Breakup in Ice–Ice Collisions. Part I: Theoretical Formulation, Journal of the Atmospheric Sciences, 74, 1705 – 1719, https://doi.org/10.1175/JAS-D-16-0224.1, 2017.

Pinder, T. and Dodd, D.: GPJax: A Gaussian Process Framework in JAX, Journal of Open Source Software, 7, 4455, https://doi.org/10.21105/joss.04455, 2022.

805 Porter, G. C. E., Sikora, S. N. F., Adams, M. P., Proske, U., Harrison, A. D., Tarn, M. D., Brooks, I. M., and Murray, B. J.: Resolving the size of ice-nucleating particles with a balloon deployable aerosol sampler: the SHARK, Atmospheric Measurement Techniques, 13, 2905–2921, https://doi.org/10.5194/amt-13-2905-2020, 2020a.

Porter, G. C. E., Sikora, S. N. F., Adams, M. P., Proske, U., Harrison, A. D., Tarn, M. D., Brooks, I. M., and Murray, B. J.: Resolving the size of ice-nucleating particles with a balloon deployable aerosol sampler: the SHARK, Atmospheric Measurement Techniques, 13,

810 2905–2921, https://doi.org/10.5194/amt-13-2905-2020, publisher: Copernicus GmbH, 2020b.

Porter, G. C. E., Adams, M. P., Brooks, I. M., Ickes, L., Karlsson, L., Leck, C., Salter, M. E., Schmale, J., Siegel, K., Sikora, S. N. F., Tarn, M. D., Vüllers, J., Wernli, H., Zieger, P., Zinke, J., and Murray, B. J.: Highly Active Ice-Nucleating Particles at the Summer North Pole, Journal of Geophysical Research: Atmospheres, 127, e2021JD036 059, https://doi.org/10.1029/2021JD036059, 2022.

Possner, A., Pfannkuch, K., and Ramadoss, V.: Cloud-Resolving ICON Simulations of Secondary Ice Production in Arctic Mixed-Phase

815 Stratocumuli Observed during M-PACE, Journal of the Atmospheric Sciences, 81, 417 – 434, https://doi.org/10.1175/JAS-D-23-0069.1, 2024.

Prévost, L. M. C., Regayre, L. A., Johnson, J. S., McNeall, D., Milton, S., and Carslaw, K. S.: Detection of structural deficiencies in a global aerosol model to explain limits in parametric uncertainty reduction, EGUsphere, 2025, 1–65, https://doi.org/10.5194/egusphere-2025-4795, 2025.

820 Proske, U., Ferrachat, S., Neubauer, D., Staab, M., and Lohmann, U.: Assessing the potential for simplification in global climate model cloud microphysics, Atmospheric Chemistry and Physics, 22, 4737–4762, https://doi.org/10.5194/acp-22-4737-2022, 2022.

Proske, U., Ferrachat, S., Klampt, S., Abeling, M., and Lohmann, U.: Addressing Complexity in Global Aerosol Climate Model Cloud Microphysics, Journal of Advances in Modeling Earth Systems, 15, e2022MS003 571, https://doi.org/10.1029/2022MS003571, 2023.

Raif, E. N., Barr, S. L., Tarn, M. D., McQuaid, J. B., Daily, M. I., Abel, S. J., Barrett, P. A., Bower, K. N., Field, P. R., Carslaw, K. S., and

825 Murray, B. J.: High ice-nucleating particle concentrations associated with Arctic haze in springtime cold-air outbreaks, EGUsphere, 2024, 1–38, https://doi.org/10.5194/egusphere-2024-1502, 2024.

Regayre, L. A., Pringle, K. J., Booth, B. B. B., Lee, L. A., Mann, G. W., Browse, J., Woodhouse, M. T., Rap, A., Reddington, C. L., and Carslaw, K. S.: Uncertainty in the magnitude of aerosol-cloud radiative forcing over recent decades, Geophysical Research Letters, 41, 9040–9049, https://doi.org/10.1002/2014GL062029, 2014.

830 Regayre, L. A., Pringle, K. J., Lee, L. A., Rap, A., Browse, J., Mann, G. W., Reddington, C. L., Carslaw, K. S., Booth, B. B. B., and Woodhouse, M. T.: The Climatic Importance of Uncertainties in Regional Aerosol–Cloud Radiative Forcings over Recent Decades, Journal of Climate, 28, 6589–6607, https://doi.org/10.1175/JCLI-D-15-0127.1, 2015.

Regayre, L. A., Johnson, J. S., Yoshioka, M., Pringle, K. J., Sexton, D. M. H., Booth, B. B. B., Lee, L. A., Bellouin, N., and Carslaw, K. S.: Aerosol and physical atmosphere model parameters are both important sources of uncertainty in aerosol ERF, Atmospheric Chemistry

835 and Physics, 18, 9975–10 006, https://doi.org/10.5194/acp-18-9975-2018, 2018.

Regayre, L. A., Deaconu, L., Grosvenor, D. P., Sexton, D. M. H., Symonds, C., Langton, T., Watson-Paris, D., Mulcahy, J. P., Pringle, K. J., Richardson, M., Johnson, J. S., Rostron, J. W., Gordon, H., Lister, G., Stier, P., and Carslaw, K. S.: Identifying climate model structural inconsistencies allows for tight constraint of aerosol radiative forcing, Atmospheric Chemistry and Physics, 23, 8749–8768, https://doi.org/10.5194/acp-23-8749-2023, 2023.

840   Renfrew, I. A. and Moore, G. W. K.: An Extreme Cold-Air Outbreak over the Labrador Sea: Roll Vortices and Air–Sea Interaction, Monthly Weather Review, 127, 2379 – 2394, https://doi.org/10.1175/1520-0493(1999)127<2379:AECAOO>2.0.CO;2, 1999.

Saltelli, A., Chan, K., and Scott, E.: Sensitivity Analysis, vol. 134, ISBN 0471998923, 2000.

Sanchez-Marroquin, A., Arnalds, O., Baustian-Dorsi, K. J., Browse, J., Dagsson-Waldhauserova, P., Harrison, A. D., Maters, E. C., Pringle, K. J., Vergara-Temprado, J., Burke, I. T., McQuaid, J. B., Carslaw, K. S., and Murray, B. J.: Iceland is an episodic source of atmospheric

845   ice-nucleating particles relevant for mixed-phase clouds, Science Advances, 6, eaba8137, https://doi.org/10.1126/sciadv.aba8137, 2020a.

Sanchez-Marroquin, A., Arnalds, O., Baustian-Dorsi, K. J., Browse, J., Dagsson-Waldhauserova, P., Harrison, A. D., Maters, E. C., Pringle, K. J., Vergara-Temprado, J., Burke, I. T., McQuaid, J. B., Carslaw, K. S., and Murray, B. J.: Iceland is an episodic source of atmospheric ice-nucleating particles relevant for mixed-phase clouds, Science Advances, 6, eaba8137, https://doi.org/10.1126/sciadv.aba8137, publisher: American Association for the Advancement of Science, 2020b.

850   Sansom, R.: Demystifying the complex nature of stratocumulus clouds with machine learning, Weather, 76, 185–191, https://doi.org/10.1002/wea.4001, 2021.

Sansom, R.: Statistical methods to understand and visualise the complex behaviour of clouds in the climate system, https://etheses.whiterose.ac.uk/id/eprint/33599/, unpublished, 2023.

Sansom, R. W. N., Carslaw, K. S., Johnson, J. S., and Lee, L.: An Emulator of Stratocumulus Cloud Response to Two Cloud-

855   Controlling Factors Accounting for Internal Variability, Journal of Advances in Modeling Earth Systems, 16, e2023MS004 179, https://doi.org/https://doi.org/10.1029/2023MS004179, 2024.

Sansom, R. W. N., Johnson, J. S., Regayre, L. A., Lee, L. A., and Carslaw, K. S.: Strong control of the stratocumulus-to-cumulus transition time by aerosol: analysis of the joint roles of several cloud-controlling factors using Gaussian process emulation, EGUsphere, 2025, 1–30, https://doi.org/10.5194/egusphere-2025-3104, 2025.

860   Sherwood, S. C., Webb, M. J., Annan, J. D., Armour, K. C., Forster, P. M., Hargreaves, J. C., Hegerl, G., Klein, S. A., Marvel, K. D., Rohling, E. J., Watanabe, M., Andrews, T., Braconnot, P., Bretherton, C. S., Foster, G. L., Hausfather, Z., von der Heydt, A. S., Knutti, R., Mauritsen, T., Norris, J. R., Proistosescu, C., Rugenstein, M., Schmidt, G. A., Tokarska, K. B., and Zelinka, M. D.: An Assessment of Earth's Climate Sensitivity Using Multiple Lines of Evidence, Reviews of Geophysics, 58, e2019RG000 678, https://doi.org/10.1029/2019RG000678, 2020.

865   Si, M., Evoy, E., Yun, J., Xi, Y., Hanna, S. J., Chivulescu, A., Rawlings, K., Veber, D., Platt, A., Kunkel, D., Hoor, P., Sharma, S., Leaitch, W. R., and Bertram, A. K.: Concentrations, composition, and sources of ice-nucleating particles in the Canadian High Arctic during spring 2016, Atmospheric Chemistry and Physics, 19, 3007–3024, https://doi.org/10.5194/acp-19-3007-2019, 2019.

Sotiropoulou, G., Sullivan, S., Savre, J., Lloyd, G., Lachlan-Cope, T., Ekman, A. M. L., and Nenes, A.: The impact of secondary ice production on Arctic stratocumulus, Atmospheric Chemistry and Physics, 20, 1301–1316, https://doi.org/10.5194/acp-20-1301-2020, 2020.

870   Steinke, I., Funk, R., Busse, J., Iturri, A., Kirchen, S., Leue, M., Möhler, O., Schwartz, T., Schnaiter, M., Sierau, B., Toprak, E., Ullrich, R., Ulrich, A., Hoose, C., and Leisner, T.: Ice nucleation activity of agricultural soil dust aerosols from Mongolia, Argentina, and Germany, Journal of Geophysical Research: Atmospheres, 121, 13,559–13,576, https://doi.org/https://doi.org/10.1002/2016JD025160, 2016.

Steinke, I., Hiranuma, N., Funk, R., Höhler, K., Tüllmann, N., Umo, N. S., Weidler, P. G., Möhler, O., and Leisner, T.: Complex plant-derived organic aerosol as ice-nucleating particles – more than the sums of their parts?, Atmospheric Chemistry and Physics, 20, 11 387–11 397,

875   https://doi.org/10.5194/acp-20-11387-2020, publisher: Copernicus GmbH, 2020.

Storelvmo, T., Tan, I., and Korolev, A. V.: Cloud Phase Changes Induced by CO2 Warming—a Powerful yet Poorly Constrained Cloud-Climate Feedback, Current Climate Change Reports, 1, 288–296, 2015.

Sullivan, S. C., Barthlott, C., Crosier, J., Zhukov, I., Nenes, A., and Hoose, C.: The effect of secondary ice production parameterization on the simulation of a cold frontal rainband, Atmospheric Chemistry and Physics, 18, 16 461–16 480, https://doi.org/10.5194/acp-18-16461-2018, 2018.

Takahashi, T., Nagao, Y., and Kushiyama, Y.: Possible High Ice Particle Production during Graupel–Graupel Collisions, Journal of Atmospheric Sciences, 52, 4523 – 4527, https://doi.org/10.1175/1520-0469(1995)052<4523:PHIPPD>2.0.CO;2, 1995.

Tarn, M., Foster, P., McQuaid, J., Robinson, J., Clarke, S., Raif, E., Choularton, T., Gallagher, M., Bower, K., Field, P., and Murray, B.: Ice-nucleating particle measurements from the M-Phase 2022 flight campaign, https://doi.org/https://doi.org/10.5281/zenodo.14781199, 2025.

Thompson, K. A.: The ice-nucleating activity of fertile soils and crop pathogens, phd, University of Leeds, https://etheses.whiterose.ac.uk/id/eprint/34821/, 2024.

Tornow, F., Ackerman, A. S., and Fridlind, A. M.: Preconditioning of overcast-to-broken cloud transitions by riming in marine cold air outbreaks, Atmospheric Chemistry and Physics, 21, 12 049–12 067, https://doi.org/10.5194/acp-21-12049-2021, 2021.

Twomey, S.: The Influence of Pollution on the Shortwave Albedo of Clouds, Journal of Atmospheric Sciences, 34, 1149 – 1152, https://doi.org/10.1175/1520-0469(1977)034<1149:TIOPOT>2.0.CO;2, 1977.

Usher, W., Herman, J., Whealton, C., Hadka, D., xantares, Rios, F., bernardoct, Mutel, C., and van Engelen, J.: SALib/SALib: Launch!, https://doi.org/10.5281/zenodo.160164, 2016.

Vali, G.: Repeatability and randomness in heterogeneous freezing nucleation, Atmospheric Chemistry and Physics, 8, 5017–5031, https://doi.org/10.5194/acp-8-5017-2008, publisher: Copernicus GmbH, 2008.

Van Weverberg, K., Giangrande, S., Zhang, D., Morcrette, C. J., and Field, P. R.: On the Role of Macrophysics and Microphysics in Km-Scale Simulations of Mixed-Phase Clouds During Cold Air Outbreaks, Journal of Geophysical Research: Atmospheres, 128, e2022JD037 854, https://doi.org/https://doi.org/10.1029/2022JD037854, 2023.

Vergara-Temprado, J., Miltenberger, A. K., Furtado, K., Grosvenor, D. P., Shipway, B. J., Hill, A. A., Wilkinson, J. M., Field, P. R., Murray, B. J., and Carslaw, K. S.: Strong control of Southern Ocean cloud reflectivity by ice-nucleating particles, Proceedings of the National Academy of Sciences, 115, 2687–2692, https://doi.org/10.1073/pnas.1721627115, 2018.

Walters, D., Boutle, I., Brooks, M., Melvin, T., Stratton, R., Vosper, S., Wells, H., Williams, K., Wood, N., Allen, T., Bushell, A., Copsey, D., Earnshaw, P., Edwards, J., Gross, M., Hardiman, S., Harris, C., Heming, J., Klingaman, N., Levine, R., Manners, J., Martin, G., Milton, S., Mittermaier, M., Morcrette, C., Riddick, T., Roberts, M., Sanchez, C., Selwood, P., Stirling, A., Smith, C., Suri, D., Tennant, W., Vidale, P. L., Wilkinson, J., Willett, M., Woolnough, S., and Xavier, P.: The Met Office Unified Model Global Atmosphere 6.0/6.1 and JULES Global Land 6.0/6.1 configurations, Geoscientific Model Development, 10, 1487–1520, https://doi.org/10.5194/gmd-10-1487-2017, 2017.

Wellmann, C., Barrett, A. I., Johnson, J. S., Kunz, M., Vogel, B., Carslaw, K. S., and Hoose, C.: Using Emulators to Understand the Sensitivity of Deep Convective Clouds and Hail to Environmental Conditions, Journal of Advances in Modeling Earth Systems, 10, 3103–3122, https://doi.org/10.1029/2018MS001465, 2018.

Wellmann, C., Barrett, A. I., Johnson, J. S., Kunz, M., Vogel, B., Carslaw, K. S., and Hoose, C.: Comparing the impact of environmental conditions and microphysics on the forecast uncertainty of deep convective clouds and hail, Atmospheric Chemistry and Physics, 20, 2201–2219, https://doi.org/10.5194/acp-20-2201-2020, 2020.

Welti, A., Bigg, E. K., DeMott, P. J., Gong, X., Hartmann, M., Harvey, M., Henning, S., Herenz, P., Hill, T. C. J., Hornblow, B., Leck, C., Löffler, M., McCluskey, C. S., Rauker, A. M., Schmale, J., Tatzelt, C., van Pinxteren, M., and Stratmann, F.: Ship-based measurements of

915   ice nuclei concentrations over the Arctic, Atlantic, Pacific and Southern oceans, Atmospheric Chemistry and Physics, 20, 15 191–15 206, https://doi.org/10.5194/acp-20-15191-2020, 2020.

Weverberg, K. V., Morcrette, C. J., and Boutle, I.: A Bimodal Diagnostic Cloud Fraction Parameterization. Part II: Evaluation and Resolution Sensitivity, Monthly Weather Review, 149, 859 – 878, https://doi.org/10.1175/MWR-D-20-0230.1, 2021a.

Weverberg, K. V., Morcrette, C. J., Boutle, I., Furtado, K., and Field, P. R.: A Bimodal Diagnostic Cloud Fraction Parameterization. Part
920   I: Motivating Analysis and Scheme Description, Monthly Weather Review, 149, 841 – 857, https://doi.org/10.1175/MWR-D-20-0224.1, 2021b.

Willett, M. R., Graham, T., Brooks, M., and Copsey, D.: GC4 and GA8GL9 acceptance report, Tech. rep., Uk Met Office, 2020.

Woodward, S., Sellar, A. A., Tang, Y., Stringer, M., Yool, A., Robertson, E., and Wiltshire, A.: The simulation of mineral dust in the United Kingdom Earth System Model UKESM1, Atmospheric Chemistry and Physics, 22, 14 503–14 528, https://doi.org/10.5194/acp-22-14503-
925   2022, 2022.

Young, G., Lachlan-Cope, T., O'Shea, S. J., Dearden, C., Listowski, C., Bower, K. N., Choularton, T. W., and Gallagher, M. W.: Radiative Effects of Secondary Ice Enhancement in Coastal Antarctic Clouds, Geophysical Research Letters, 46, 2312–2321, https://doi.org/10.1029/2018GL080551, 2019.

Zelinka, M. D., Myers, T. A., McCoy, D. T., Po-Chedley, S., Caldwell, P. M., Ceppi, P., Klein, S. A., and Taylor, K. E.: Causes of Higher Cli-
930   mate Sensitivity in CMIP6 Models, Geophysical Research Letters, 47, e2019GL085 782, https://doi.org/10.1029/2019GL085782, 2020.